An experimental speciation study of DME, OME$_1$, and OME$_2$ in a single-pulse shock tube at high pressures

Fabian Lindner [a,b,*], Marina Braun-Unkhoff [b,#], Clemens Naumann [b], Torsten Methling [b], Markus Köhler [b], Uwe Riedel [c]

[a] University of Stuttgart, Institute of Combustion Technology for Aerospace Engineering, Stuttgart, Germany
[b] German Aerospace Center (DLR), Institute of Combustion Technology, Stuttgart, Germany
[c] German Aerospace Center (DLR), Institute of Low-Carbon Industrial Processes, Cottbus, Germany

ARTICLE INFO

ABSTRACT

The pyrolysis of dimethyl ether (DME), oxymethylene ether-1 (OME$_1$), and oxymethylene ether-2 (OME$_2$) and their oxidation with oxygen under three different equivalence ratios ($\varphi = 0.5$, 1.0, and 2.0) have been studied experimentally in a customized single-pulse shock tube. The measurements were carried out highly diluted in argon over a wide temperature range between 975 K and 1400 K at initial pressures behind reflected shock waves $p_5(t = 0)$ of about 16 bar. The classical single-pulse mode involving a dump tank was not employed. Instead, post-shock gas samples were extracted through a fast-acting solenoid valve located inside the end flange of the driven section of the shock tube, to reduce measurement errors from thermal boundary layers. Thirteen stable species were identified and quantified by three different gas chromatographs simultaneously, in detail, DME, OME$_1$, OME$_2$, methane, ethane, ethene, acetylene, carbon monoxide, carbon dioxide, molecular hydrogen, formaldehyde, methanol, and methyl formate. The temperature dependent, measured, and normalized species concentration profiles were compared with the predicted species profiles obtained by using two different chemical kinetic reaction mechanisms from the literature and an updated version of the in-house reaction model DLR Concise. In addition, speciation data of 1,1,1-trifluoroethane and nitrous oxide at elevated pressures are presented, which were used as external chemical thermometers to validate the calculated temperature behind the reflected shock wave of the single-pulse shock tube.

Novelty and Significance: In this work, a series of more than 300 single-pulse shock tube experiments have been performed, to investigate the decomposition products of oxygenated fuels at pressures around 16 bar. To the best of our knowledge, no speciation data is yet available for this pressure regime. By comparing the data with chemical-kinetic reaction mechanisms from the literature, opportunities for model improvement have been identified, particularly regarding methanol formation, which could be further developed in the future.

The presented high-pressure validation data contributes to the development of chemical-kinetic reaction models for new oxygenated fuels derived from renewable sources. By incorporating these reaction mechanisms into CFD codes, advancements in combustors and engine technology are facilitated, promoting cleaner combustion processes.

1. Introduction

In 2015, at the Conference of Parties in Paris (COP 21), 196 parties declared 'The Paris Agreement', aiming to minimize the harmful effects of global warming by limiting the man-made temperature increase to 2 °C or even 1.5 °C above pre-industrial levels [1]. Achieving this goal will require a massive reduction of greenhouse gas (GHG) emissions and,

even more, of carbon dioxide equivalents (CO$_2$-eq), a metric used to compare the emissions from different greenhouse gases based on their global-warming potential (GWP). The transport sector is responsible for a large proportion of global greenhouse gas emissions [2] due to its current predominant use of fossil fuels. In addition to the effects of water vapor and CO$_2$, further contributions to the greenhouse effect are linked to nitrous oxide (N$_2$O) and unburned hydrocarbons (UHC), such as

methane (CH_4) [3], while emissions of nitrogen oxide (NO_x), carbon monoxide (CO), and soot additionally pose additional risk to human health and the environment [4–6].

Synthetic fuels produced from renewable sources could contribute to a significant net reduction of anthropogenic emissions. For the ground transport sector, oxygenated fuels, among others, have been widely discussed in the literature for their potential to replace fossil fuels – neat or in blends [7–9]. Among the most promising candidates are oligomers of polyoxymethylene dimethyl ethers (OME_n, $CH_3O(CH_2O)_nCH_3$, where $n \geq 0$). Several studies at various blending ratios of OME_n in diesel have demonstrated nearly soot-free combustion, which also allows to escape from the trade-off between NO_x and soot formation usually encountered in compression ignition (CI) engines [10–13].

Understanding the fundamental combustion properties of these oxygenated fuels enables the development of detailed chemical kinetic reaction mechanisms, which are required for numerical calculations and general assessment strategies in engine development and optimization to ensure a safe and clean use of OME_n as fuels. For this purpose, experimental data under different conditions are essential to cover a wide range of combustion boundary conditions. For dimethyl ether (DME or OME_0), experimental data and modeling studies are available in the literature [14–24], while experimental data for larger OME_n, [22–32], are quite limited, especially at high pressures.

In the present study, the oxygenated fuels DME, OME_1, and OME_2 were investigated for the pyrolysis and oxidation at three fuel-equivalence ratios $\varphi = 0.5$ (fuel-lean), 1.0 (stoichiometric), and 2.0 (fuel-rich). The measurements were performed highly diluted in argon in a single-pulse shock tube at initial fuel concentrations of about 500 ppm over a wide temperature range between 975 K and 1400 K and at initial pressures behind reflected shock waves $p_5(t = 0)$ of about 16 bar. A customized experimental setup of the DLR's single-pulse shock tube [33] was used, without employing the classical single-pulse mode involving a dump tank [34]. Instead, post-shock gas samples were extracted into a small and evacuated volume through a fast-acting solenoid valve located inside the end flange of the driven section of the shock tube. The product distribution of the post-shock gas samples was analyzed simultaneously by three different gas chromatographs (GC). A total number of thirteen stable species were identified and quantified. In addition, the experimental results were compared with the predictions of three detailed chemical kinetic reaction mechanisms, including an updated version of the in-house developed semi-detailed reaction mechanism DLR Concise [35], which includes reactions of polyoxymethylene dimethyl ethers up to OME_5.

2. Experimental setup

2.1. Mixture preparation

The gas mixtures were prepared in a 65.7-liter stainless steel vessel that was electrically heated up to 373 K. It was evacuated to 3.0×10^{-5} mbar by a pumping system that includes a turbo pump and a diaphragm pump. The concentrations of the test gas mixtures used in this work were adjusted using partial pressures. Mixtures of DME (purity: 99.9%, Linde), 1,1,1-trifluoroethane (purity: 99.5%, Westfalen AG) as well as nitrous oxide (purity: 99.999%, Linde) were prepared manometrically by filling a certain amount of gas into a small sample volume of 55 ml and then flushed into the evacuated mixing vessel with a mixture of 4950 ppm xenon in argon (Linde, purity: 99.998% (Xe) and 99.9999% (Ar), respectively) and oxygen (O_2, purity: 99.9999%, Linde). Mixtures of OME_1 and OME_2 were prepared by injecting a weighed amount of OME_1 or OME_2 in liquid form directly into the evacuated mixing vessel using a syringe. Xenon/argon and oxygen were then added manometrically to achieve the desired dilution. To ensure a homogeneous gas mixture, all mixtures were left to mix overnight. OME_1 was purchased from Sigma Aldrich (purity: 99.0%) and OME_2 from Analytik-Service GmbH (ASG, purity: 96.0%). Minor impurities of OME_1,

formaldehyde, methanol, and methyl formate were detected in OME_2 (96.0% OME_2, 2.1% OME_1, 1.2% formaldehyde, 0.6% methanol, 0.1% methyl formate).

2.2. Apparatus

The customized single-pulse shock tube (see Fig. 1) is designed to analyze stable product patterns at post-shock pressures of up to 40 bar and temperatures ranging from 700 K and 3000 K. It is constructed from stainless steel and can be electrically heated up to 473 K to prevent condensation of the fuel and of the combustion products on the inner wall. However, since the fast-acting solenoid valve used for gas sampling has a maximum operating temperature of 378 K, the shock tube in this study was heated up to 373 K. Both ends of the shock tube are closed by an end flange. A 10 cm long double aluminum diaphragm assembly forms the intermediate section, dividing the shock tube into a 2.42 m long driver section and a 4.89 m long driven section. The entire shock tube has an inner diameter of 4.6 cm. Before each experiment, the driven section is evacuated to pressures of about 1.5×10^{-5} mbar by a turbo-molecular pump coupled to a rotary vane pump. The driver section and the intermediate section are connected to a rotary vane pump, which reaches a pressure of less than 1.0×10^{-3} mbar. Helium (purity: 99.996%, Linde) is used as the driver gas.

To start a specific experiment, the intermediate section (see Fig. 1) is evacuated, causing both aluminum membranes to burst, creating a shock wave that propagates along the driven section. Eight piezoelectric pressure transducers (type: PCB 112A05) are used to measure the velocity of the incident shock wave. The temperature and pressure behind the reflected shock wave (T_5 and p_5) are calculated by the ideal one-dimensional equations for the shock jump condition [36] by using the shock wave velocity at the end flange. The shock wave velocity at the end flange is estimated by measuring the attenuating velocity along the driven section and its linear extrapolation to the end flange position. This standard practice results in an uncertainty of $\pm 1\%$ for T_5 [37].

The classical single-pulse mode involving a dump tank [34] was not employed. Instead, a fast-acting solenoid valve (First Sensor series 9 Pulse Valves, type: 9S2-A1-P3-9B06) is mounted inside the end flange of the shock tube's driven section. A probe protrudes 3 mm off from the end wall surface of the end flange inside the driven section of the shock tube to ensure sampling outside the thermal boundary layer [38,39]. A similar approach was published recently by Ferris et al. [40].

The fast-acting solenoid valve is connected to a sample volume of 13.7 ml. The sampling event is initiated approximately 3 ms after the arrival of the incident shock wave at the end flange; it is triggered by a delayed ($\sim$ 5.6 ms) signal from the fourth piezoelectric pressure transducer to the fast-acting solenoid valve assuming quenched conditions after this time interval (dwell time) due to an 20% pressure drop of the pressure profile measured 10 mm before the end flange (Fig. 2 at $t \sim 2.6$ ms, black dashed curve). This assumption is based on literature recommendations [41,42] and an expected temperature drop of 0.5 to 1 K/μs [43] induced by the superposition of the reflected rarefaction fan and the decompression wave created when the reflected shock wave passes through the contact surface. The pressure profile inside the shock tube displayed in Fig. 2 corresponds to a shock tube experiment using 100% argon, with $T_5 = 1181$ K and $p_5 = 16.0$ bar. The slight pressure reduction within the first millisecond after the reflection of the incident shock wave is attributed to an irregular burst of the double-aluminum diaphragm arrangement, a phenomenon that occurred occasionally.

The sampling time ends after approximately 7.4 ms, which is represented by a peak of the pressure rise in the sample volume (Fig. 2 at $t \sim$ 10 ms, red solid curve, 120 mbar $< p_{sample} <$ 180 mbar), measured by a piezoelectric pressure transducer (type: PCB 113A21) in a separate series of experiments. Note that the pressure profile, dwell time, and sampling time are unique and may vary with respect to T_5 and p_5. In all cases, the fast-acting solenoid valve has to be completely closed before the re-reflected shock wave arrives again at the end flange of the driven
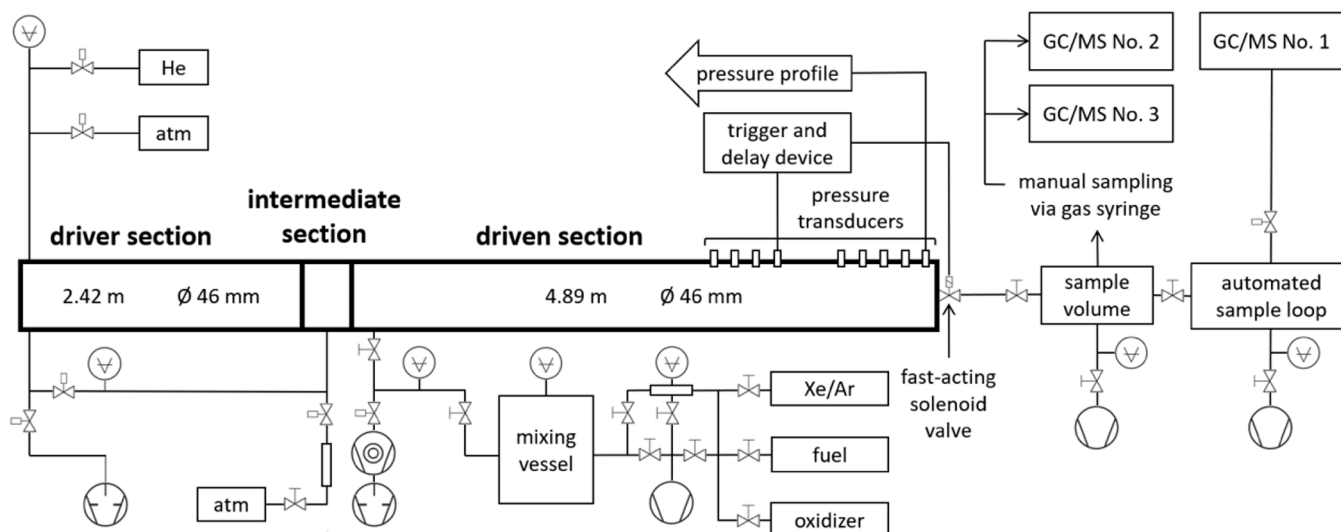
Fig. 1. Sketch of the DLR single-pulse shock tube. The fast-acting solenoid valve is located inside the end flange of the driven section of the shock tube and is connected to an evacuated small volume. Three different GCs each coupled with a MS and mounted with different separation columns are used to analyze the product distribution of post-shock gas samples.
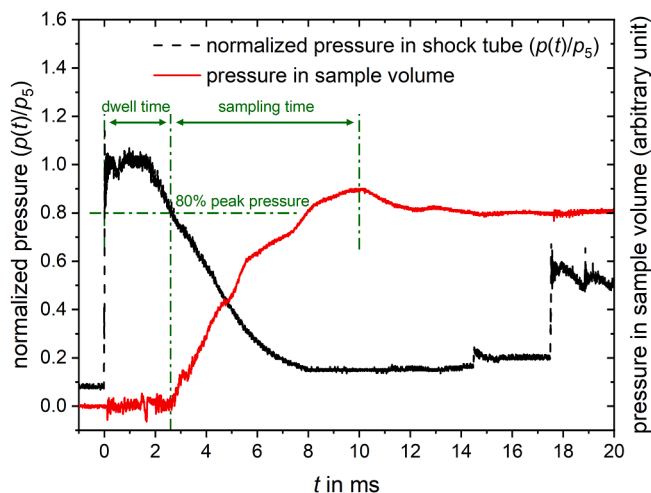

Fig. 2. Normalized pressure profile $p(t)/p_5$ in the shock tube, measured 10 mm in front of the end flange of the driven section (black dashed curve) and pressure profile in the sample volume with the valve fully opened (red solid curve) to determine the optimum sampling time.

section (Fig. 2 at $t \sim 17.5$ ms) since no dump tank [34] is used in the present setup and to prevent the gas sample being taken out again from the decompression event.

The pressure signals were recorded using an oscilloscope (Tektronix TBS2204B) with 200 MHz bandwidth, 8-bit vertical resolution, and a sample rate of 2 GSa/s. To smooth the pressure profile before incorporating it into the numerical simulations, a Savitzky-Golay filter was applied.

2.3. Sample analysis

Post-shock gas samples are analyzed using three different gas chromatographs simultaneously, each equipped with a different separation column and coupled to a mass spectrometer. GC/MS No. 1 (GC 2010 Plus with QCMS-QP2020 from Shimadzu) is directly connected to the sample volume via a sample loop and is equipped with a non-polar Rt®-Q-BOND PLOT separation column from Restek (used for N_2O, 1,1,1-trifluoroethane, 1,1-difluoroethene, DME, methane, ethane, ethene,

acetylene, and CO_2). Sample volume and sample loop are heated up to 373 K to prevent condensation of post-shock products. Both are connected to a separate pumping system consisting of a turbo drag-pump backed by a diaphragm pump achieving pressures of 4.0×10^{-2} mbar and 1 mbar, respectively. GC/MS No. 2 (GC 2010 with QCMS-QP2010 Plus from Shimadzu) and GC/MS No. 3 (GC 2010 Plus with QCMS-QP2010 Ultra from Shimadzu) are mounted with a Zebron™ ZB-WAX-plus™ polar column by Phenomenex (used for OME_1, OME_2, formaldehyde, methanol, and methyl formate) and a Rt®-Msieve 5A column by Restek (used for H_2 and CO), respectively. Gas samples for GC/MS No. 2 and No. 3 are injected manually by a gas syringe, that is stored in an oven at 393 K prior to injection to avoid condensation of gas products. Gases and chemicals used to calibrate the GCs were obtained by different suppliers. Linde delivered methane (purity: 99.9995%), ethane (purity: 99.95%), ethene (purity: 99.95%), acetylene (purity: 99.6%) in gas mixtures of alkanes, alkenes or alkynes (diluted in nitrogen to concentrations of around 500 ppm), molecular hydrogen (purity: 99.999%), carbon monoxide (purity: 99.997%) and carbon dioxide (purity: 99.9993%). 1,1-Difluoroethene (purity: 99.0%) and methyl formate (purity: 99%) were purchased from Sigma Aldrich. Methanol (purity: 99.8%) was obtained by Merck. Gas mixtures of formaldehyde were prepared by pyrolysis of paraformaldehyde (thermo scientific, purity: 96.0%) at T > 110 °C. Helium (Linde, purity: 99.9999%) is used as carrier gas for all GCs and xenon as the internal standard.

3. Kinetic modeling

The chemical kinetic simulations are calculated using a 0-dimensional homogeneous reactor model implemented in the SENKIN-Code of the Chemkin II package [44]. For each individual simulation, the corresponding experimentally obtained pressure profile $p = p(t)$, which was smoothed using a Savitzky-Golay filter, is used as an input for the calculations to account for the post-shock compression pressure rise due to gas dynamic effects. A figure demonstrating this phenomenon can be found in the Supplementary Material. The reaction time is defined to be between the arrival of the reflected shock wave at the end flange of the driven section and the time when an 20% pressure drop of the experimentally obtained pressure profile is observed, assuming that most of the reactions are quenched by freezing conditions. However, to account for all recombination reactions, the simulation time was defined as the sum of the dwell time and the sampling time ($t = t_{dwell} + \Delta t_{sampling}$). Since no significant concentration gradients were observed in the

individual species after a specific simulation time (see Fig. S3 in the Supplementary Materials), the final simulation time was set to 8 ms. The mole fractions were then extracted at this time and used for comparison with experimental results.

The calculations with DME, OME₁, and OME₂ as fuels were performed using three chemical kinetic reaction mechanisms from the literature, listed in Table 1. This selection includes an updated version of our in-house reaction model DLR Concise [35]. In this update, the recently published jet fuel mechanism 'DLRConcise2021v1.JF' [45] is modified and updated, *e.g.*, (i) by adding low-temperature combustion chemistry for OME_{0-5} and also for *n*-heptane and *iso*-octane, and (ii) by introducing nitrogen chemistry from the mechanism of Glarborg et al. [46] with reactions of OME_n-NO_x interaction to allow prediction of NO_x emissions for OME_n. For clarification, the new model is here referred to as 'DLRConcise2024v2.F'.

4. Chemical thermometry

In this work, two external chemical thermometers [49,50] were used to investigate the temperature behind the reflected shock wave. Knowing the exact temperature is critical to obtain accurate results in single-pulse shock tube studies [37]. Here, the thermal decomposition of a molecule, for which the reaction rate expressions are well known and well studied in literature, is used in order to obtain a more accurate temperature history of the gas mixture. There are two general strategies described in the literature: Internal and external chemical thermometers. The internal chemical thermometers are present directly in the gas mixture itself, but may lead to side reactions with the molecule to be studied. External chemical thermometers are studied separately over a wide range of temperatures and can be used for comparison as long as the conditions, *e.g.* pressure profile and dilution, are comparable. Regarding the design of an individual experimental facility, the results of both methods subsequently confirm [51,52], correct [33,41,53–57] or replace [58,59] the specific temperature, which is calculated by the equations of the shock jump condition [36] from the measured shock wave velocity.

First, the decomposition of nitrous oxide (N_2O) has been examined in the present work, which has already been considered as an external chemical thermometer by Schuler et al. [33] who sampled at a radial port through the boundary layer. In our investigated temperature range between 1222 K and 1637 K, the main reaction leading to consumption of N_2O is the unimolecular thermal decomposition of N_2O, which produces molecular nitrogen (N_2) and an O atom. The rate coefficients of this reaction found in the literature have mostly been studied by precise time-resolved optical measurement methods [60], *e.g.*, IR spectroscopy in a laminar flow reactor by Johnsson et al. [61]. In addition, the results were reviewed by Baulch et al. [60] and have been incorporated to the mechanism by Glarborg et al. [46] as well as to the model by Konnov [62]. Therefore – and because of further reactions with decomposition products that may contribute to a further consumption of N_2O ($N_2O + O \leftrightarrow N_2 + O_2$, $N_2O + O \leftrightarrow 2\,NO$, and $N_2O + NO \leftrightarrow NO_2 + N_2$) although with minor priority (see ROP in Fig. S4) – we have used the mechanism of Glarborg et al. [46] and the newest version of the Konnov mechanism [62] for the calculated model predictions of N_2O. A discussion of the comparison between the calculated and the measured yield of N_2O within our experimental setup is given later.

Second, the unimolecular thermal decomposition of 1,1,1-trifluoroethane (TFE, CH_3CF_3) to 1,1-difluoroethylene (DFE, CH_2CF_2) and

hydrogen fluoride (HF) was investigated in a temperature range between 1173 K and 1430 K. Numerous single-pulse shock tube studies in the literature have considered TFE as chemical thermometer [41,51, 53–59] or have investigated the thermal decomposition of TFE itself [63–68] driven by the need to accurately predict the temperature behind the reflected shock wave. Currently, two mechanisms are considered in literature: The one of Tsang and Lifshitz [63] and that of Matsugi et al. [67] and Matsugi [68]. Recently, Sirjean et al. [54] questioned the reaction rate coefficients reported by Tsang and Lifshitz [63] based on single-pulse shock tube measurements. Matsugi et al. [67] also found the coefficients of Tsang and Lifshitz [63] to be too high in a discussion involving other experimental data [54,63–66,69]. Consequently, Matsugi et al. [67] and Matsugi [68] published new rate coefficients based on shock tube/laser absorption spectroscopy and single-pulse shock tube methods combined with RRKM/master equation calculations. Although the reaction rate coefficients of Matsugi et al. [67] and Matsugi [68] are now considered in the literature to be the most plausible, they are also occasionally debated [51,70,71]. Furthermore, a third mechanism was published by Giri and Tranter [65]; this model was obtained from experimental data gathered from their own single-pulse shock tube/time of flight mass spectrometry (TOF-MS) measurements and from the shock tube/laser-schlieren (LS) measurements of Kiefer et al. [64].

In the present work, while studying the unimolecular thermal decomposition of TFE, we additionally tracked the concentration of the resulting DFE. This molecule undergoes partial consumption through the subsequent reaction CH_2CF_2 (+ M) $\leftrightarrow$ CHCF + HF (+ M). We observe its impact on our experimental finding by a slight flattening in the trend of the DFE data at higher temperatures. Matsugi et al. [67] provide rate coefficients also for the decomposition of DFE. Giri and Tranter [65] included the rate coefficients by Simmie and Tschuikow-Roux [72]. Tsang and Lifshitz [63] did not include DFE decomposition pathways into their model. Therefore, we modified the Tsang and Lifshitz model by adding the DFE decomposition reaction step and rate coefficients proposed by Simmie and Tschuikow-Roux [72].

5. Results and discussion

5.1. Chemical thermometry: nitrous oxide and 1,1,1-trifluoroethane

First, we examine the speciation measurements of the thermal decomposition of nitrous oxide (N_2O) and 1,1,1-trifluoroethane (TFE)
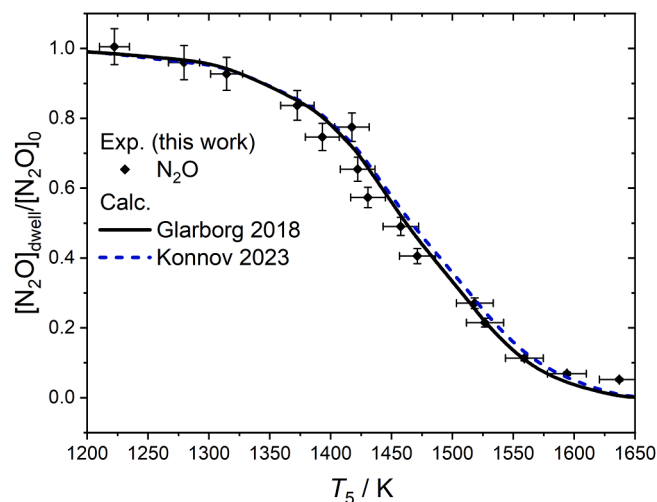
Fig. 3. Normalized mole fractions of the thermal decomposition of approximately 502 ppm nitrous oxide (N_2O) diluted in argon at pressures around 16 bar. Experiment (this work): Diamond; calculations: Solid curves using the kinetic model by Glarborg et al. [46], dashed curves using the model by Konnov et al. [62].

Table 1
Overview of the chemical kinetic models used in this work.

Reaction Model	Species	Reactions
DLRConcise2024v2.F [35]	290	1225
Cai et al. 2020 [47]	322	1611
Shrestha et al. 2022 [48]	259	1678

shown in Figs. 3 and 4, respectively. Both molecules serve as chemical thermometers; they were separately studied at initial concentrations of about 500 ppm diluted in argon (Linde, purity: 99.9999%) at pressures of $p_5 = 16.2$ bar ($\pm$ 0.6 bar) over a wide range of temperatures. As an internal standard, a mixture of 30,000 ppm xenon in helium (Linde, purity: 99.99% (Xe) and 99.9993% (He), respectively) was added manometrically to the sample volume after every experiment. It was then left for mixing for at least 30 min. Note that this procedure was modified later on when studying the depletion of the three ethers by adding xenon as internal standard directly into the intended ether mixture. The measured concentrations after the dwell time ([TFE]$_{dwell}$, [DFE]$_{dwell}$, and [N$_2$O]$_{dwell}$) are shown in normalized form relative to the initial concentration, [N$_2$O]$_0$ or [TFE]$_0$, respectively, as a function of the initial temperature $T_5(t = 0)$ – the temperature behind the reflected shock wave. Measurement uncertainties are also provided in the graphs.

Uncertainty in measuring the velocity of the incoming shock wave contributes to the temperature uncertainty (abscissa), which results in $\pm$1% of T_5. The uncertainty of the individual concentration (ordinate) is calculated through error propagation [71,73], taking into account the standard deviation of the calibration factor for each species, the purity uncertainties of the test gases according to the manufacturer's specification, and the uncertainties in the evaluation of the individual peaks in the chromatogram of the gas chromatograph.

The deviation between experimental and calculated data can only be estimated for the temperature range in which the chemical thermometer is sensitive, *i.e.*, the temperatures at which thermal decomposition can be observed. For our experimental setup, this is about 1275 K to 1600 K for N$_2$O and about 1150 K to 1400 K for TFE, respectively. In the temperature range for N$_2$O, the experimental and modeled results are in good agreement (Fig. 3). Some minor deviations are observed in the temperature range between 1393 K and 1470 K; however, they are within the error tolerances. Based on this observation, within the temperature range covered by the N$_2$O decomposition, the temperature calculated by the one-dimensional shock jump equation [36] can be reasonably assumed to be the temperature actually experienced by the gas mixture. Therefore, no temperature corrections are required based on the N$_2$O measurements.

Fig. 4 shows the experimental data and the model predictions of the

thermal decomposition of TFE and formation of DFE. All thermodynamic data are taken from Goos et al. [74]. For our experimental setup, the sensitivity of this reaction system is in the temperature range around 1150 K to 1400 K. Regarding the TFE results, the mechanism by Tsang and Lifshitz [63] reproduces our experimental data quite well for low temperatures (Fig. 4, solid curves). With increasing temperature, an increasing deviation is observed, where the TFE consumption appears to be too fast predicted by the mechanism of Tsang and Lifshitz [63], with a maximum deviation of approximately 30 K. However, with respect to the mechanism proposed by Giri and Tranter [65] (Fig. 4, dotted curves) the TFE consumption is predicted too slow and a temperature correction of about 25 K towards higher temperatures is required. On the other hand, the model of Matsugi et al. [67] and Matsugi [68] (Fig. 4, dashed curves) predicts an even slower decomposition and necessitates a temperature correction of 50 K towards higher temperatures. Due to the estimation of Matsugi et al. [67] – reporting that the rate coefficients by Tsang and Lifshitz [63] were too high – and the widely accepted mechanism by Matsugi et al. [67] and Matsugi [68], the present experimental results are deemed unsatisfying in this context. The DFE data demonstrate a similar trend of disparities between experimental data and model prediction because DFE is a direct decomposition product of TFE. The formation of DFE is overpredicted by Tsang and Lifshitz [63] and underpredicted by Matsugi et al. [67] and Matsugi [68] when compared to our experimental data. Nevertheless, the prediction of Giri and Tranter [65] aligns well with our results, if error tolerances were considered.

When comparing the results of TFE and N$_2$O, an overlap is observed in the temperature range between around 1275 K to 1400 K, in which both chemical thermometers are sensitive (see Fig. S5). While there was good agreement observed within the N$_2$O data in this temperature range, the TFE data necessitates a temperature correction, leading in two distinct conclusions for the same temperature range.

It may be suggested to use a non-linear temperature correction that matches the temperature range of the N$_2$O measurements and corrects the temperature range for the TFE data. However, introducing such a correction is not straightforward if there is no agreement on the overlapping temperature range on the TFE and N$_2$O data, which is between 1275 K and 1400 K. Additionally, it is challenging to explain why the gas would encounter a temperature higher than what is calculated by the one-dimensional shock jump equation [36]. Usually, the opposite is observed [75] – 'real' gas temperatures are lower than those calculated by the shock jump equation [36] due to heat dissipation along the shock tube or boundary layer effects. However, these effects are largely minimized by our experimental design. An excessively high temperature correction could undermine the accuracy of calculating the temperature via the one-dimensional shock jump equation [36]. Consequently, implementing a non-linear temperature correction is not reasonable.

To allow a more objective decision about the need and the extend of a temperature correction, a chi-square distribution ($\chi^2 = \sum_{i=1}^{n}(\sigma_{exp,i} - \sigma_{mod,i})^2/error^2(\sigma_{exp,i})$) was calculated (see Fig. S6). Based on this analysis, we apply the following two-step strategy: (1) Examine our pyrolysis measurements of dimethyl ether with two different temperature profiles mirroring the results of the chemical thermometers (*i.e.*, TFE/DFE: $T_{5,real} = T_{5,calc} + 45$ K and N$_2$O: No temperature shift); then (2), use the chemical kinetic mechanisms including the in-house model DLR Concise [35], the mechanism by Cai et al. [47], and the mechanism by Shrestha et al. [48] to validate the species profiles in this study.

Fig. 5 shows the procedure described with using experimental results and model predictions of the pyrolytic decomposition of DME. The results are presented as [DME]$_{dwell}$ normalized to the initial concentration [DME]$_0$ plotted against the initial temperature $T_5(t = 0)$ behind the reflected shock wave. Experimental results without a temperature shift are shown as full squares, whereas those with a temperature shift of +45 K are indicated as open squares. Model predictions are denoted by solid curves for our in-house model DLR Concise [35], dashed curves for the
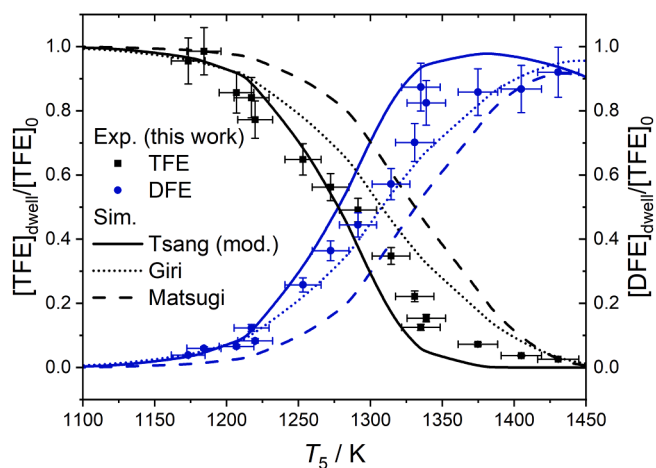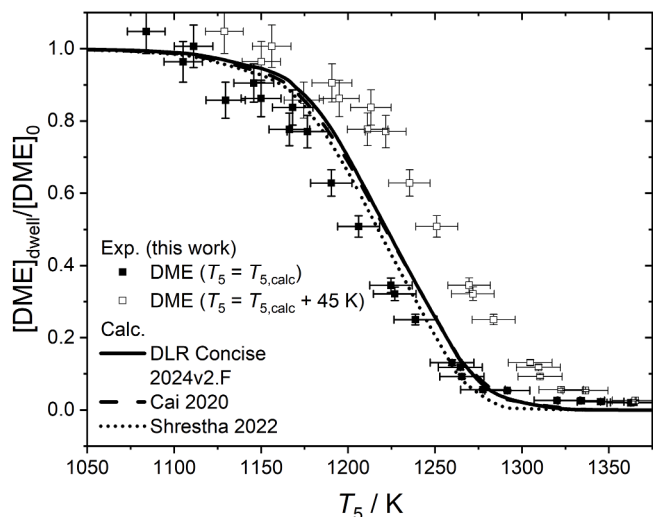

Fig. 4. Normalized mole fractions of the thermal decomposition of approximately 500 ppm 1,1,1-trifluoroethane (TFE) diluted in argon at pressures around 16 bar. In addition, 1,1-difluoroethylene (DFE) was monitored as decomposition product. Experiments (this work): Black squares (TFE), blue circles (DFE); calculations: Solid curves using the model by Tsang and Lifshitz [63] with added rate coefficient data for DFE decomposition obtained from Simmie and Tschuikow-Roux [72], dotted curves using the model by Giri and Tranter [65], and dashed curves using the model by Matsugi et al. [67] and Matsugi [68]. The reaction rate coefficient data used for the calculations are given in Table S2 of the Supplementary Material.

Fig. 5. Normalized mole fractions of the pyrolysis of approximately 500 ppm DME diluted in argon with 4950 ppm xenon at pressures around 16 bar. Experiment (this work): Filled squares (DME – no temperature shift), open squares (DME – with a temperature shift of +45 K); calculations: Solid curves (DLRConcise2024v2.F [35]), dashed curves (Cai et al. [47]), and dotted curves (Shrestha et al. [48]).

Cai et al. [47] mechanism, and dotted curves for the Shrestha et al. [48] mechanism. All models are validated against extensive experimental data sets for the pyrolysis and oxidation of DME. We do not want to anticipate the kinetic discussion of DME at this point, and therefore refer to the later section for this matter. Nonetheless, Fig. 5 clearly shows that all three mechanisms considered show a clear trend towards those experimental data points without the positive temperature correction.

Based on the results of the N_2O measurements as a chemical thermometer and the comparison of the dimethyl ether measurements with predictions using chemical kinetic mechanisms from the literature – it was decided not to make any temperature corrections for the species profiles discussed in this work. To ensure clarity, we considered the temperature calculated by the one-dimensional shock jump equation [36] as the actual temperature experienced by the gas mixture at the start of the compression event. It is important to note that for each individual model calculation the corresponding experimentally obtained pressure profile $p = p(t)$ is used as input to account for temperature changes caused by individual pressure fluctuations.

5.2. Pyrolysis of DME, OME₁, and OME₂

The initial concentration of each fuel for the pyrolysis, as well as for the three different oxidative conditions discussed later, was kept
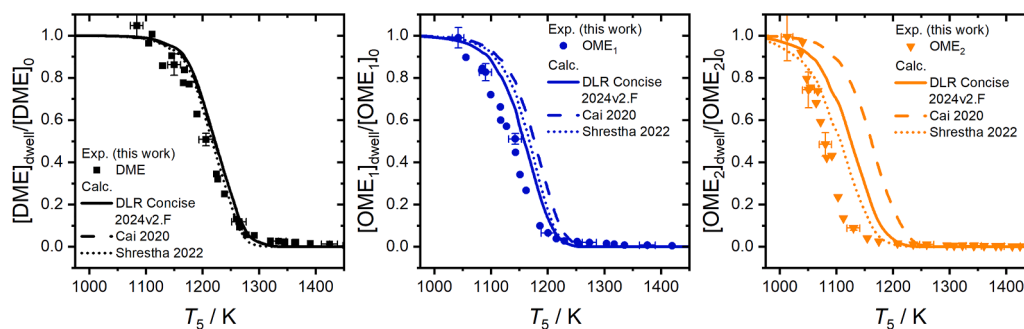
constant at 500 ppm (489 ppm for OME₂). This approach consequently results in a decreasing dilution as the mixing ratio moves from pyrolytic to fuel-rich, stoichiometric, and fuel-lean conditions, due to the increasing oxygen content (see Table S3 for more information on mixtures and experimental conditions). For OME₂, small amounts of impurities of decomposition products were detected (96.0% OME₂, 2.1% OME₁, 1.2% formaldehyde, 0.6% methanol, 0.1% methyl formate), which were considered in the simulations as initial concentrations.

Fig. 6 shows the experimental results and model predictions of the pyrolytic decomposition of DME, OME₁, and OME₂ after the dwell time ([Fuel]$_{dwell}$). As with the chemical thermometers in the previous section, the mole fractions are shown normalized to the initial concentration of the individual molecule ([Fuel]$_0$) *versus* the initial temperature $T_5(t = 0)$ behind the reflected shock wave. For a better readability, uncertainty limits (see previous section) are displayed only in a certain temperature interval although actually present for each data point.

Comparing the three fuels shown in Fig. 6 it is seen that as the chain length of the corresponding oxygenated molecules increases, the onset of decomposition starts at lower temperatures. This characteristic is related to the decreasing bond dissociation energies (BDE) of C–O and C–H bonds in each molecule as the chain length [76] increases, coupled with the increasing likelihood of a bond breaking. For example, the bond dissociation energy of the C–O bond for DME is 83.2 kcal/mol [77], while OME₁ and OME₂ have primary bond dissociation energies of 80.61 kcal/mol [76] and 79.8 kcal/mol [76], respectively. For OME₁ and OME₂, and higher OMEs, BDEs are higher at the secondary carbon atom than at the primary carbon atom [76]. This can be attributed to an electron shift due to the higher electronegativity of oxygen as compared to carbon; as a result, chain start reactions are more probable at the primary carbon atom [78].

Based on rate of progress (ROP) analysis performed, the initial reaction for the pyrolysis of DME is the unimolecular decomposition $CH_3OCH_3 (+ M) \leftrightarrow CH_3O + CH_3 (+ M)$ forming a methoxy radical (CH_3O) and a methyl radical (CH_3). The CH_3O stabilizes to CH_2O (formaldehyde) and releases a hydrogen radical, which is the dominant path leading to CH_2O. The released H atom may subsequently interconnect with the existing radical pool through recombination reactions such as combining with another hydrogen radical to form H_2 or reacting with CH_3 to form CH_4 (methane). It may also react with DME via H-abstraction reactions as indicated by $CH_3OCH_3 + H \leftrightarrow CH_3OCH_2 + H_2$. In addition, H-abstraction reactions via $CH_3OCH_3 + CH_3 \leftrightarrow CH_3OCH_2 + CH_4$ are vital in high temperature DME decomposition. The dominant subsequent decomposition of methoxymethyl radicals occurs through β-scission via $CH_3OCH_2 \leftrightarrow CH_2O + CH_3$, another important reaction that forms CH_2O.

The experimental speciation data for pyrolysis of DME is consistent with all three models. However, Shrestha et al. [48] is slightly closer to the measured data, probably a result of the rate coefficients used for H-abstraction reactions with DME via H. Shrestha et al. [48] obtained

Fig. 6. Normalized mole fractions of the pyrolysis of approximately 500 ppm fuel diluted in argon with 4950 ppm xenon at pressures around 16 bar. Experiment (this work): Black squares (DME), blue circles (OME₁), and orange triangles (OME₂); Calculations: Solid curves (DLRConcise2024v2.F [35]), dashed curves (Cai et al. [47]), and dotted curves (Shrestha et al. [48]).

the reaction rates of DME + H from the work of Sivaramakrishnan et al. [79], which are slightly accelerated compared to the reaction rates from Burke et al. [80]. The latter are implemented in the DLR Concise model [35] and the mechanism by Cai et al. [47].

Seven stable species were detected and quantified during the pyrolysis of DME. These include methane, ethane, ethene, ethyne, carbon monoxide, H_2, and formaldehyde, as shown in Fig. 7. The primary reaction forming methane is $CH_2O + CH_3 \leftrightarrow CH_4 + HCO$. As the temperature increases, additional reactions contribute to the formation of methane via H-abstraction reactions of CH_3 with DME, H_2, and C_2H_6 as well as via the recombination reaction of $CH_3 + H$. Two additional reactions compete with methane formation: The production of ethane via $2\ CH_3\ (+ M) \leftrightarrow C_2H_6\ (+ M)$, and the dehydrogenation of formaldehyde via $CH_2O + H \leftrightarrow HCO + H_2$ acting as both an H-atom scavenger and a CH_2O scavenger. A slight flattening in the trend of the methane data at temperatures higher than 1260 K is observed. At this temperature, the fuel consumption of DME is about 87% implying that the CH_3 supply via CH_3OCH_3 and CH_3OCH_2 decomposition is about to collapse. Furthermore, CH_2O as the main H-donor for CH_4 formation is largely consumed at this temperature. However, methane concentration continues to steadily increase at temperatures above 1260 K, although with a lower slope. This finding can be related to the decreasing supply of CH_3 via DME decomposition as well as the additional but minor supply of

CH_3 at higher temperatures via ethane decomposition: $C_2H_6\ (+ M) \leftrightarrow 2\ CH_3\ (+ M)$. Competing to this reaction, ethane also decomposes via dehydrogenation reactions to form ethene and subsequently ethyne. No additional higher hydrocarbons were detected.

All mechanisms show good agreement for the detected hydrocarbons, with the model of Shrestha et al. [48] being closest to the data for methane. However, the predicted ethane concentrations from the same model are slightly above the experimental data due to the utilization of faster reaction rate coefficients for $2\ CH_3\ (+ M) \leftrightarrow C_2H_6\ (+ M)$ from Baulch et al. [60]. The DLR Concise model [35] includes rate coefficients for $2\ CH_3\ (+ M) \leftrightarrow C_2H_6\ (+ M)$ obtained by Wang et al. [81], whereas the mechanism of Cai et al. [47] includes data taken from Oehlschlaeger et al. [82]. Best fit for the ethane data is obtained through the mechanism of Cai et al. [47]. It is important to note that all mechanisms used here have different core mechanisms. Specifically, (i) the H_2-O_2 chemistry from Burke et al. [83] along with a carefully considered compilation of C_1–C_5 species for the DLR Concise [35]; (ii) the C_0–C_4 mechanism is taken from Blanquart et al. [84] and implemented in the model of Cai et al. [47], and (iii) sub-models for C_0 [85] and C_1–C_2 [86] in the model of Shrestha et al. [48] were derived from previous publications by their group mainly following the recommendations of Baulch et al. [60].

A large amount of formaldehyde was detected, which is formed via $CH_3O\ (+ M) \leftrightarrow CH_2O + H\ (+ M)$ and $CH_3OCH_2 \leftrightarrow CH_2O + CH_3$. With
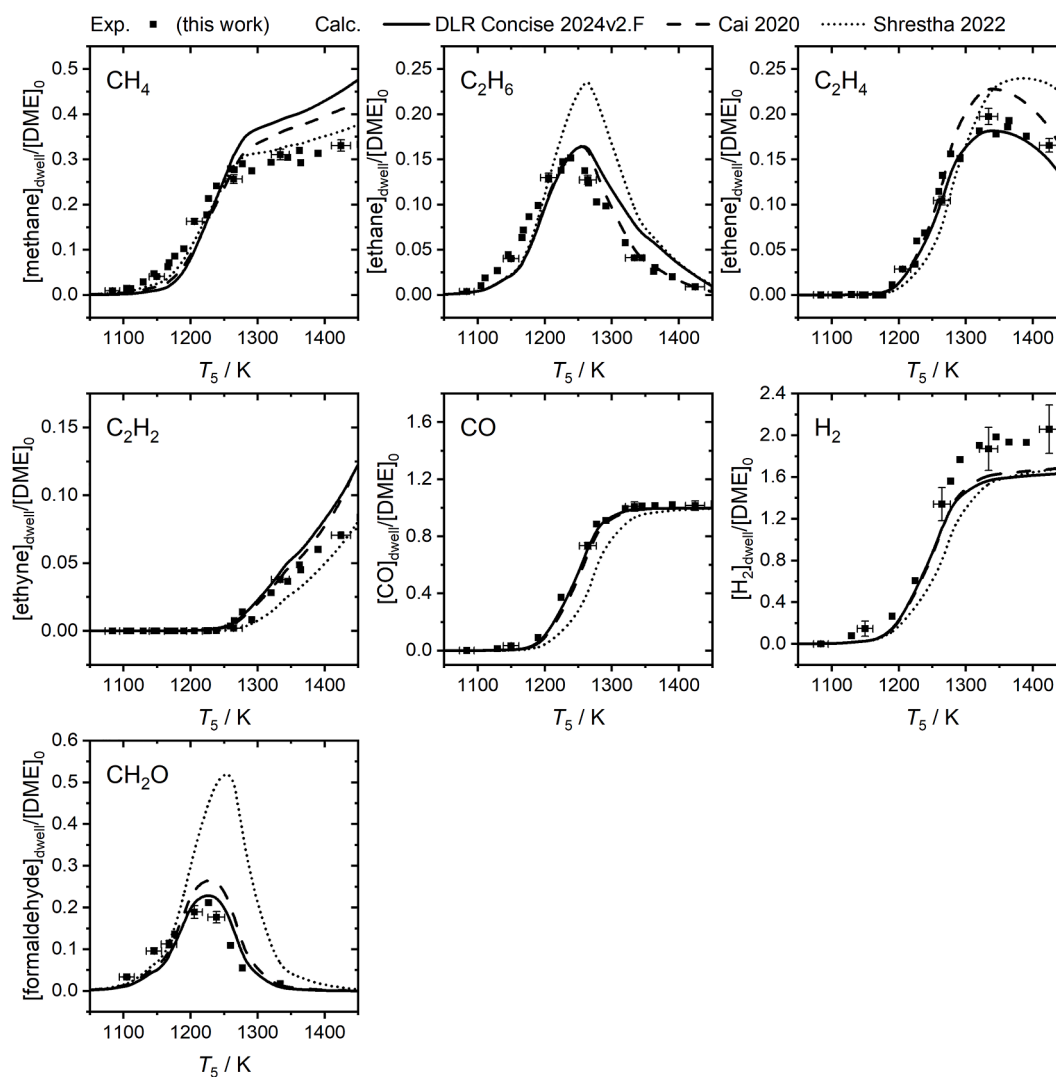

Fig. 7. Normalized species profiles of the decomposition products for the pyrolysis of approximately 500 ppm DME diluted in argon with 4950 ppm xenon at pressures around 16 bar. Experiment (this work): Black squares; calculation: Solid curves (DLRConcise2024v2.F [35]), dashed curves (Cai et al. [47]), and dotted curves (Shrestha et al. [48]).

increasing temperatures, CH_2O primarily decomposes via H-abstraction reactions to form HCO. Friedrichs et al. [87] identified the competing unimolecular decomposition reaction $CH_2O (+ M) \leftrightarrow CO + H_2 (+ M)$ as part of the high temperature decomposition of CH_2O. However, due to its high activation energy and the large amount of radicals in our system, this reaction plays only a minor role in our CH_2O decomposition experiments. Instead, a high amount of HCO is produced, which itself decomposes rapidly [87] mainly through H-cleavage to form $CO + H$. The DLR Concise model [35] and the model by Cai et al. [47] align well with the formaldehyde data observed experimentally. In contrast, the model of Shrestha et al. [48] overpredicts the respective data. This is primarily due to the implementation of slower reaction rate coefficients for $CH_2O + H \leftrightarrow HCO + H_2$ from Baulch et al. [60], in contrast to those in the other two mechanisms which are taken from the work of Irdam et al. [88]. Consequently, the model of Shrestha et al. [48] predicts a slower increase in CO data as a result of the reduced slower decomposition rate of formaldehyde.

Furthermore, a large amount of molecular hydrogen is formed via recombination or H-abstraction reactions involving atomic hydrogen in several reactions. Due to mass conservation, the deviation between the calculated and experimental data is opposite to those species previously observed; H_2 profiles are underpredicted by the mechanisms, while most of the other species data containing hydrogen are overpredicted.

In summary, the agreement between the three extensively validated models and the experimental results in this work is satisfactory. This demonstrates the reliability of our measurement method including the determination of the temperature behind the reflected shock wave as well as the simulation methodology based on the pressure profile.

Regarding the pyrolysis of OME_1 shown in Fig. 6, the measured mole fraction decomposition occurs faster than predicted by each of the three investigated mechanisms. This results in a deviation of about 20 to 30 K, with the in-house DLR Concise model [35] showing slightly closer results to the experimental data. According to the studies by Golka et al. [78], OME_1 predominantly undergoes decomposition via C–O bond fission of the primary carbon atom – also denoted as primary channel – forming $CH_3 + CH_3OCH_2O$. CH_3OCH_2O then reacts via H-cleavage to form CH_3OCHO (methyl formate) or via β-scission to form CH_2O and CH_3O. A secondary channel forms $CH_3O + CH_3OCH_2$ by C–O bond fission of the secondary carbon atom. In the recently published work of Pazdera et al. [89], the authors discussed the existence of eight additional competing unimolecular decomposition reactions of OME_1. In the mechanisms discussed in the present work merely four more unimolecular reactions can be found; however, only two of them result in a significant contribution to the decomposition of OME_1: $OME_1 (+ M) \leftrightarrow CH_2O + DME (+ M)$ and $OME_1 (+ M) \leftrightarrow CH_3OH + CH_3 + HCO (+ M)$. The last reaction might play an important role as we observed a large amount of methanol formed during the experiments. It should be noted that methanol is also be produced by the unimolecular decomposition of methyl formate forming $CH_3OH + CO$. H-addition reactions of CH_3O to form CH_3OH should be negligible here since a large amount of CH_3O was also formed in our DME measurements, but almost no yield of CH_3OH was detected.

Furthermore, H-abstraction reactions with OME_1 occur either at the primary carbon atom forming $CH_3OCH_2OCH_2$ which reacts further via β-scission to CH_3OCH_2 and CH_2O or at the secondary carbon atom forming $CH_3OCHOCH_3$ which reacts further via β-scission to CH_3OCHO and CH_3. Cai et al. [47] and Shrestha et al. [48] also considered both reactions as unimolecular decomposition via H-cleavage; however, due to the much higher BDE of the C–H bonds compared to those of the C–O bonds, both reactions are negligible for the temperature range investigated in this work.

The three model predictions of the OME_1 pyrolysis, differ slightly from each other, as they use different sub-mechanisms for OME_1 with varying expressions. In more detail, the DLR Concise model [35] uses a set of selected rate values for OME_1, which are obtained from He et al. [90], Sun et al. [76], De Ras et al. [91], Golka [92], Shrestha et al. [48],

and Cai et al. [47], while the mechanism of Cai et al. [47] itself uses a sub-mechanism for OME_1, which is based on the model by Jacobs et al. [93]. The OME_1 data in the mechanism of Shrestha et al. [48] consists of their recent work of Shrestha et al. [94], in which most of the reaction rates were obtained from model studies by Vermeire et al. [95], Sun et al. [96], Jacobs et al. [93], and Sun et al. [76]. Furthermore, the DLR Concise model [35] and the model by Shrestha et al. [48] favor the secondary channel over the primary one (see ROP in Fig. S8), which is supported, *e.g.*, by the work of Vermeire et al. [95] and Peukert et al. [97], but contradicted by the recently published work of Golka et al. [78] and Pazdera et al. [89]. Both studies revealed the reaction $OME_1 (+ M) \leftrightarrow CH_3 + CH_3OCH_2O (+ M)$ as the dominating reaction above temperatures of 900 K, which is consistent when comparing the amount of the corresponding BDEs. Moreover, the temperature shift observed between the experimental data and the model predictions of OME_1 is consequently also reflected in the profiles of its decomposition products (see Fig. 8), in particular of methane, ethane, and methyl formate, albeit with the exception of formaldehyde. The measurements of hydrocarbons are mostly in good agreement with the model predictions, although they vary among themselves; however, the modeled data for CO, hydrogen, and formaldehyde are largely overpredicted. Regarding CO, the deviation between experimental and modeled concentrations at higher temperatures may imply that the missing mass must be present in other species. Since CO contains oxygen, oxygenated compounds are of particular relevance. While OME_1, methyl formate, and formaldehyde are nearly fully depleted under these conditions, small amounts of methanol remain. However, the concentration of methanol does not fully account for the discrepancy, and the small quantity of CO_2 produced is also insufficient to offset the observed mass loss. Nevertheless, the strong agreement between the experimental and modeled CO data during the pyrolysis of DME supports the reliability of the CO measurements within this work. This observation, along with a C/H/O balance calculation (see Supplementary Materials) suggests that not all species generated during the pyrolysis of OME_1 were detected. It is likely that additional, unidentified species – such as acetaldehyde, ethanol, water, or others – as well as alternative reaction pathways, may be influencing the observed mass distribution.

Additionally, the yield of methyl formate from our experimental data is in good agreement with the model predictions, while the predictions of methanol are underpredicted. This may indicate a previously underestimated reaction that produces methanol independently from methyl formate.

Fig. 6 shows the measured and modeled mole fractions of OME_2, while the species profiles of the decomposition products are given in Fig. 9. Our experimental data for OME_2 mole fractions are in good agreement with the model predictions of Shrestha et al. [48] with slightly increasing deviation as the temperature rises; some larger deviations are observed compared to the DLR Concise model [35] and even more regarding the predictions by the model from Cai et al. [47].

Analogous to OME_1, OME_2 may decompose via a primary channel forming $CH_3 + CH_3OCH_2OCH_2O$, and via a secondary channel forming $CH_3O + CH_3OCH_2OCH_2$ (see OME_1 discussion). Regarding the primary channel, $CH_3OCH_2OCH_2O$ decomposes via formaldehyde elimination to CH_3OCH_2O (see OME_1 discussion) or reacts via H-cleavage to methoxymethyl formate (CH_3OCH_2OCHO); however, no methoxymethyl formate was identified in our experiments, although this molecule was recently traced as minor intermediate by De Ras et al. [91,98] in a tubular quartz reactor under pyrolytic conditions using two-dimensional gas chromatography (GC × GC) coupled with flame ionization detection (FID) and mass spectroscopy (MS). Furthermore, due to the additional methoxy group in the chemical structure of OME_2, an additional channel might exist via C–O bond fission of the central oxygen atom forming $CH_3OCH_2 + CH_3OCH_2O$. Analogous to OME_1, the methanol forming reaction $OME_2 (+ M) \leftrightarrow CH_3OH + HCO + CH_3OCH_2 (+ M)$ is implemented in our mechanism and in the mechanism of Shrestha et al. [48], while Shrestha et al. [48] also included the reactions $OME_2 (+ M) \leftrightarrow$
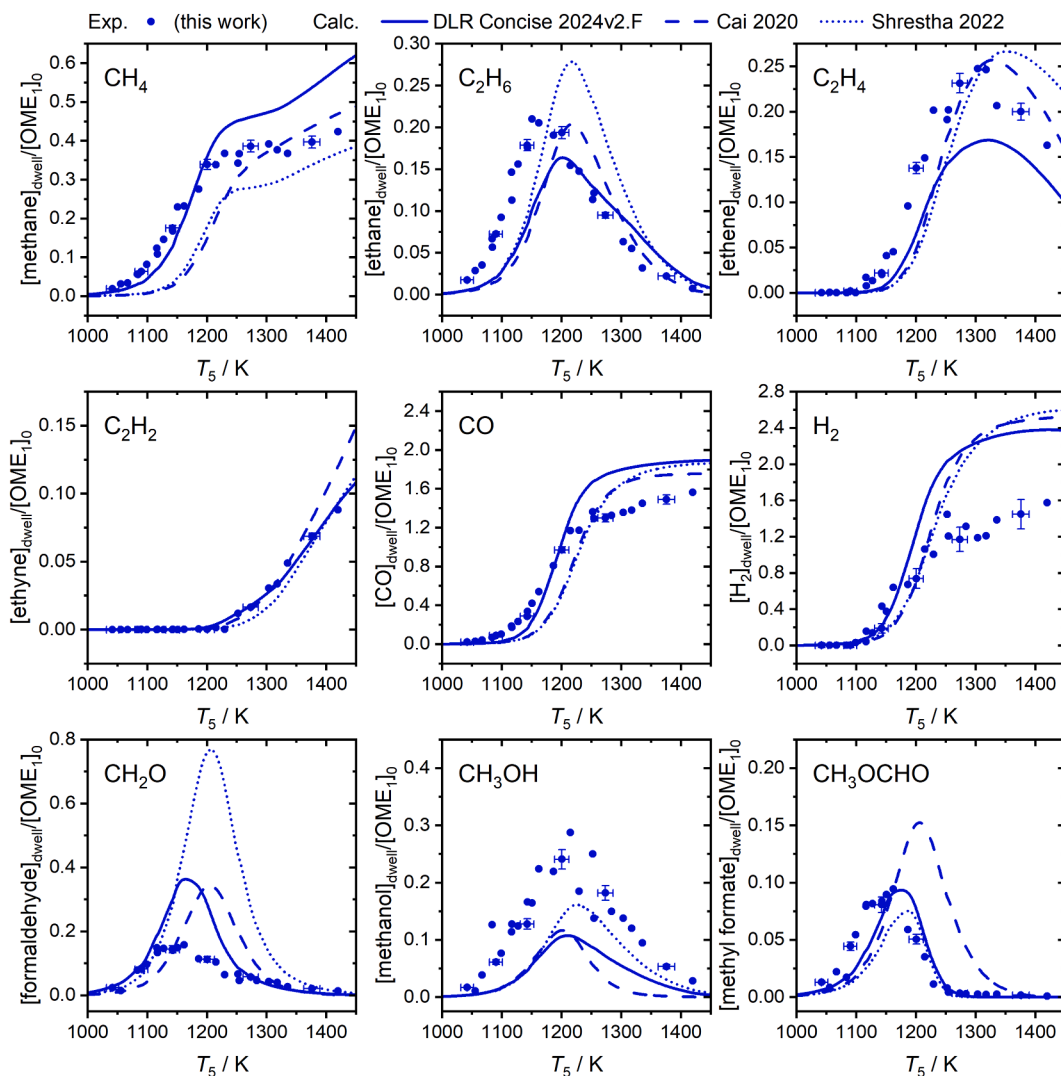
Fig. 8. Normalized species profiles of the decomposition products for the pyrolysis of approximately 500 ppm OME_1 diluted in argon with 4950 ppm xenon at pressures around 16 bar. Experiment (this work): Full circles; calculation: Solid curves (DLRConcise2024v2.F [35]), dashed curves (Cai et al. [47]), and dotted curves (Shrestha et al. [48]).

OME_1 + formaldehyde (+ M), as well as OME_2 (+ M) ↔ CH_3OCH_2OH + HCO + CH_3 (+ M). However, once again, no CH_3OCH_2OH (methoxymethanol) was detected during our measurements, yet in small amounts in the experiments by De Ras et al. [91,98].

H-abstraction reactions from OME_2 at the primary and secondary carbon atom occur; these reactions are also implemented as H-cleavage reactions in the mechanism of Cai et al. [47] and Shrestha et al. [48] yielding $CH_3OCH_2OCH_2OCH_2$ via the primary channel and CH_3O-$CH_2OCHOCH_3$ via the secondary channel. The only reaction found in all three mechanisms, which results in a decomposition of CH_3OCH_2O-CH_2OCH_2 is the formaldehyde elimination forming $CH_3OCH_2OCH_2$. $CH_3OCH_2OCHOCH_3$ may react to methyl formate releasing CH_3OCH_2 or to methoxymethyl formate releasing CH_3.

Due to the lack of literature studies investigating the reaction rates of OME_2 experimentally, most of the reaction rate expressions of the decomposition and H-abstraction reactions found in the three mechanisms were obtained either from quantum chemical calculations [91] or estimated by analogies with DME, OME_1, diethoxymethane (DEM, $(C_2H_5O)_2CH_2$) [99], and diethyl ether (DEE, $(C_2H_5)_2O$) [100].

Regarding the obtained methane data, again some deviations with respect to the model predictions are observed; however, the results of Shrestha et al. [48] are in good agreement at temperatures lower than 1200 K. With higher temperatures, the experimental methane data are underpredicted by the model of Shrestha et al. [48] and overpredicted by the DLR Concise model [35] and the mechanism of Cai et al. [47].

Model predictions for ethane, ethene, and ethyne are slightly underestimated, with most significant deviations observed at ethene data for the DLR Concise model [35]. Moreover, the onset of ethane and ethyne formation is slightly shifted to higher temperatures, despite the fact that methane and ethane are both formed via CH_3 radicals. CO and H_2 mole fractions are overpredicted by all the mechanisms considered, with the smallest deviations observed for the model of Cai et al. [47]. The onset of formaldehyde formation agrees fairly well with the predictions of the DLR Concise model [35] and the one by of Shrestha et al. [48] with respect to our experimental data. Both mechanisms favor the secondary channel for OME_2 decomposition, OME_2 (+ M) ↔ CH_3O + $CH_3OCH_2OCH_2$ (+ M), in which CH_3O is formed as a formaldehyde precursor. However, both mechanisms overpredict the measured formaldehyde profiles at temperatures above 1100 K. Considering the predictions by using the model of Cai et al. [47], both the peak value as well as the shape of the modeled formaldehyde data fit well with the experiments, despite a temperature shift of about 60 K. Similar to the pyrolysis of OME_1, a large amount of methanol has been detected during our experiments. Since the model of Cai et al. [47] does not consider the
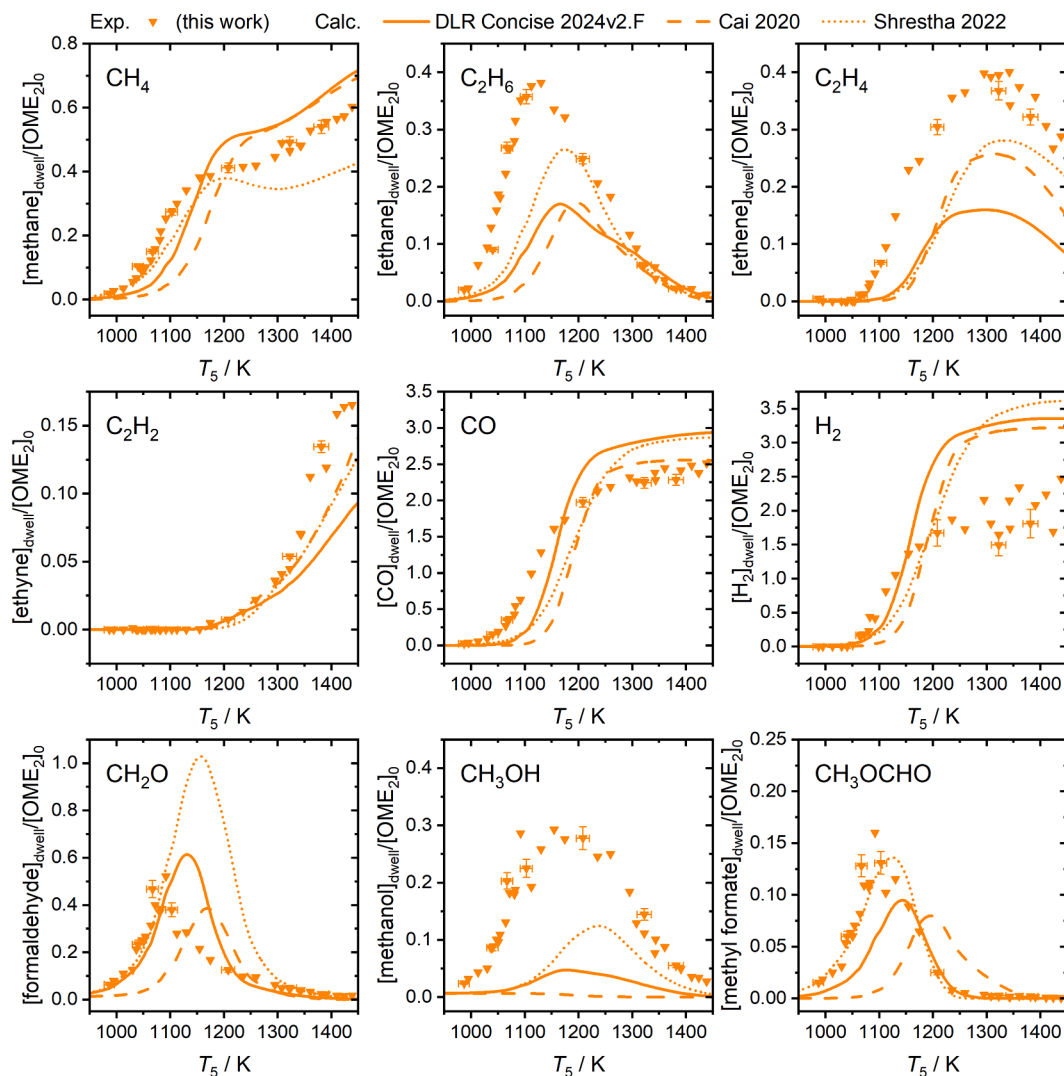
Fig. 9. Normalized species profiles of the decomposition products for the pyrolysis of approximately 489 ppm OME_2 diluted in argon with 4950 ppm xenon at pressures around 16 bar. Experiment (this work): Orange circles; calculation: Solid curves (DLRConcise2024v2.F [35]), dashed curves (Cai et al. [47]), and dotted curves (Shrestha et al. [48]).

methanol forming reaction $OME_2 (+ M) \leftrightarrow CH_3OH + HCO + CH_3OCH_2$ $(+ M)$, almost no increase in the methanol mole fraction is therefore calculated. Even in the DLR Concise model [35] and the model of Shrestha et al. [48], which both include the corresponding reaction, the measured methanol mole fractions are still underpredicted. In addition,

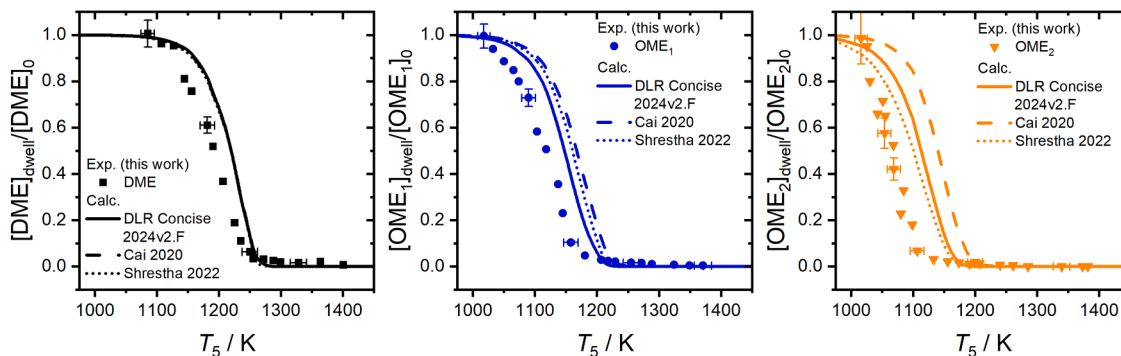the methyl formate profile is matched by using the model of Shrestha et al. [48].

Fig. 10. Normalized mole fractions of the oxidation ($\varphi = 1.0$) of approximately 500 ppm fuel diluted in argon with 4950 ppm xenon at pressures around 16 bar. Experiment (this work): Black squares (DME), blue circles (OME_1), and orange triangles (OME_2); calculation: Solid curves (DLRConcise2024v2.F [35]), dashed curves (Cai et al. [47]), and dotted curves (Shrestha et al. [48]).

5.3. Oxidation of DME, OME$_1$, and OME$_2$

Within this work, the oxidation of DME, OME$_1$, and OME$_2$ was also investigated using the same experimental method, by exploiting stoichiometric conditions, fuel-lean, and fuel-rich mixtures with oxygen diluted in argon with xenon. We focus on the discussion of the findings on stoichiometric conditions ($\varphi = 1.0$), with occasionally referring to all fuel-oxygen mixtures. The measurements performed under fuel-rich ($\varphi = 2.0$) and fuel-lean ($\varphi = 0.5$) conditions are given in the Supplemental Material (Fig. S13 – S20), together with the corresponding numerical calculations.

Fig. 10 shows the experimental results and the model predictions for DME, OME$_1$, and OME$_2$ with 1500, 2000, and 2500 ppm O$_2$, respectively, to obtain stoichiometric ($\varphi = 1.0$) mixture conditions. Compared to the results for the pyrolysis of the corresponding fuels displayed in Fig. 6, both the experimental data as well as the modeling results are slightly shifted towards lower temperatures. This increased reactivity of the stoichiometric mixtures is due to the additional reactions with O$_2$ and the resulting larger radical pool encompassing O, OH, and HO$_2$ radicals enhancing the decomposition of the corresponding fuel. According to the rate coefficients of Burke et al. [101], the production of

radicals and consequently the fuel consumption as well as the consumption of stable species and intermediates are determined by the competition between the chain-branching reaction H + O$_2$ ↔ O + OH increasing the mixture's reactivity and the recombination reaction H + O$_2$ (+ M) ↔ HO$_2$ (+ M) reducing the reactivity of the gas mixture by firstly scavenging an H radical and secondly by forming HO$_2$ which reacts more slowly compared to OH. Considering the rate coefficients of both reactions included in the three mechanisms considered in the present work for the numerical calculation of the species profiles, as well as the high pressure conditions in our experiments, the reaction pathway in which OH is formed is favored for temperatures above 1250 K when using the DLR Concise model [35], 1245 K when using the model of Cai et al. [47], and 1235 K for Shrestha et al. [48]. It should be mentioned that, due to the high dilution in argon, in addition those reactions identified in the pyrolysis of the fuel (via unimolecular decomposition) also significantly affect the fuel consumption under oxidative conditions.

Looking at the species data for DME obtained under stoichiometric conditions ($\varphi = 1.0$) as shown in Fig. 11, the rise in the experimentally determined methane concentration is steeper compared to those observed under pyrolytic conditions; this finding is not seen in the
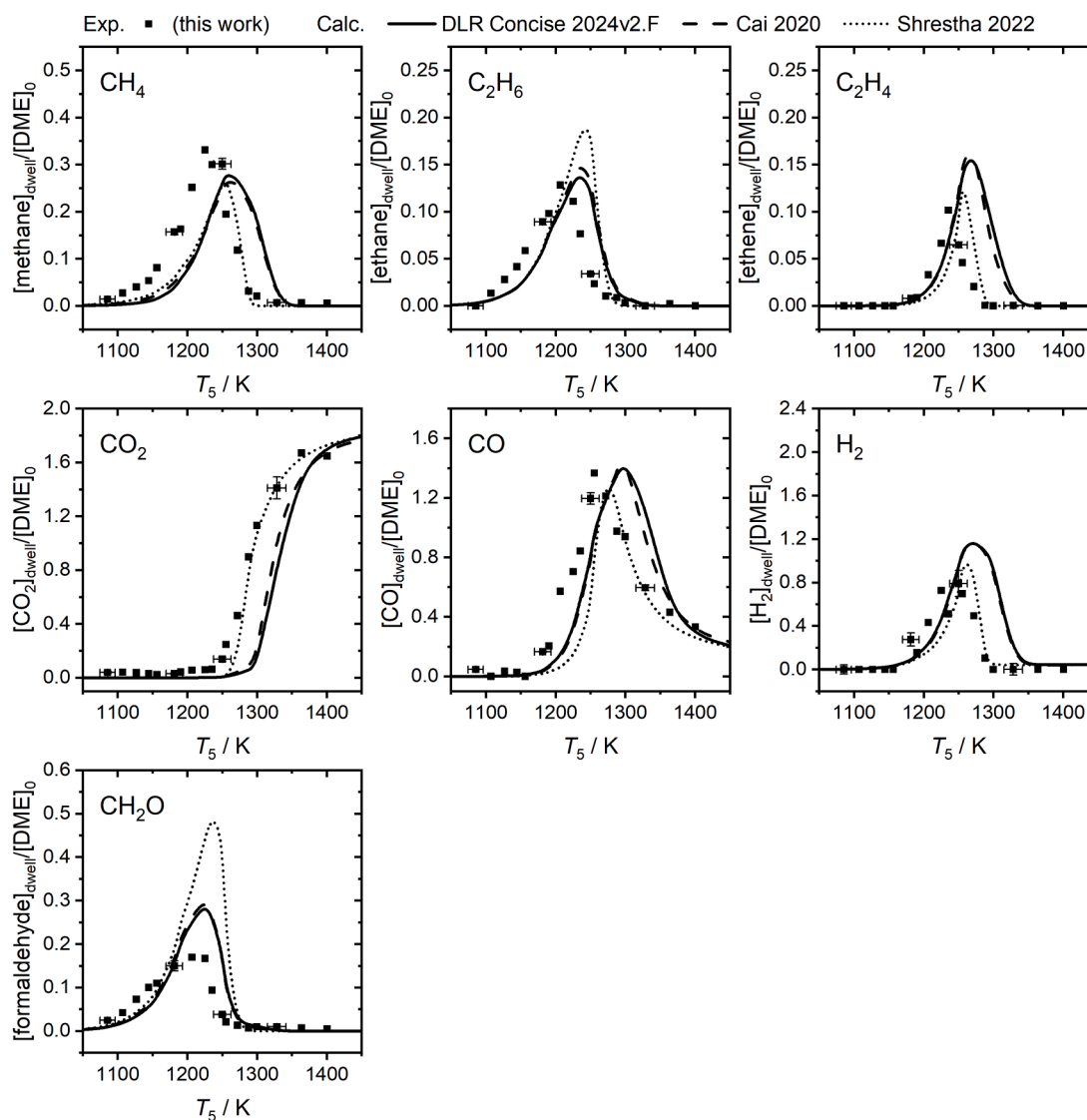

Fig. 11. Normalized species profiles of the decomposition products for the oxidation ($\varphi = 1.0$) of approximately 500 ppm DME diluted in argon with 4950 ppm xenon at pressures around 16 bar. Experiment (this work): Black squares; calculation: Solid curves (DLRConcise2024v2.F [35]), dashed curves (Cai et al. [47]), and dotted curves (Shrestha et al. [48]).

modeling. On the one hand – due to the experimentally observed faster DME decomposition (see Fig. 10) – also CH_3 radicals are already available at lower temperatures and may form methane. On the other hand – the presence of HO_2 functions as an additional H-donor to form methane, although its effect via $CH_3 + HO_2 \leftrightarrow CH_4 + O_2$ should be weak because the competing reaction $CH_3 + HO_2 \leftrightarrow CH_3O + OH$ dominates [102], and no increase in formaldehyde data is observed compared to pyrolytic conditions. Furthermore, at temperatures above 1250 K, a rapid decomposition of methane is seen; this is due to two reasons: (i) A reduction in CH_3 supply as DME and formaldehyde are largely consumed; and (ii) – even more important – a drastic increase of methane consumption via the H-abstraction reactions $CH_4 + O \leftrightarrow CH_3 + OH$ and $CH_4 + OH \leftrightarrow CH_3 + H_2O$ since the OH forming channel via $H + O_2 \leftrightarrow O + OH$ begins to dominate. Regarding the measurements under fuel-rich ($\varphi = 2.0$) and fuel-lean ($\varphi = 0.5$) mixture conditions (see Fig. S14 and Fig. S18), the drop in the respective methane concentration shifts slightly to higher temperatures for mixtures with lower oxygen content ($\varphi = 2.0$), and moves to lower temperatures for mixtures with higher oxygen content (fuel-lean, $\varphi = 0.5$), since a higher concentration of oxygen leads to the formation of more OH. Note that the dilution of the mixture changes with increasing oxygen content, which slightly affects the highly pressure-dependent reaction $H + O_2 (+ M) \leftrightarrow HO_2 (+$

M) due to changing collision efficiencies, and thus, ultimately the temperature at which $H + O_2 \leftrightarrow OH$ becomes dominant. Since the dominance of the OH forming channel occurs at slightly lower temperatures in the model of Shrestha et al. [48] compared to the other two mechanisms, the collapse in the methane concentration is consequently also observed at somewhat lower temperatures and therefore fits better with the experimental results.

The same effect can also be seen in the drop in concentrations for the ethene and hydrogen data at the same temperatures. Except for DME under fuel-rich ($\varphi = 2.0$) conditions, no ethyne data or other higher hydrocarbons were detectable under oxidative conditions. Compared to pyrolysis, a higher amount of CO concentrations was measured, as CO is also formed by the oxidation of the hydrocarbons in addition to the reaction path via formaldehyde. However, above temperatures of 1255 K, CO begins to be consumed as well via reactions with O and OH radicals to form CO_2, which is reflected by an enormous increase in the CO_2.

In conclusion, all three mechanisms show good agreement compared with the stoichiometric, fuel-rich, and fuel-lean DME speciation profiles, but indicate a slightly slower DME decomposition. The predictions of Shrestha et al. [48] are the closest to the experimental data, especially at higher temperatures; however, they overpredict the formaldehyde species profiles.
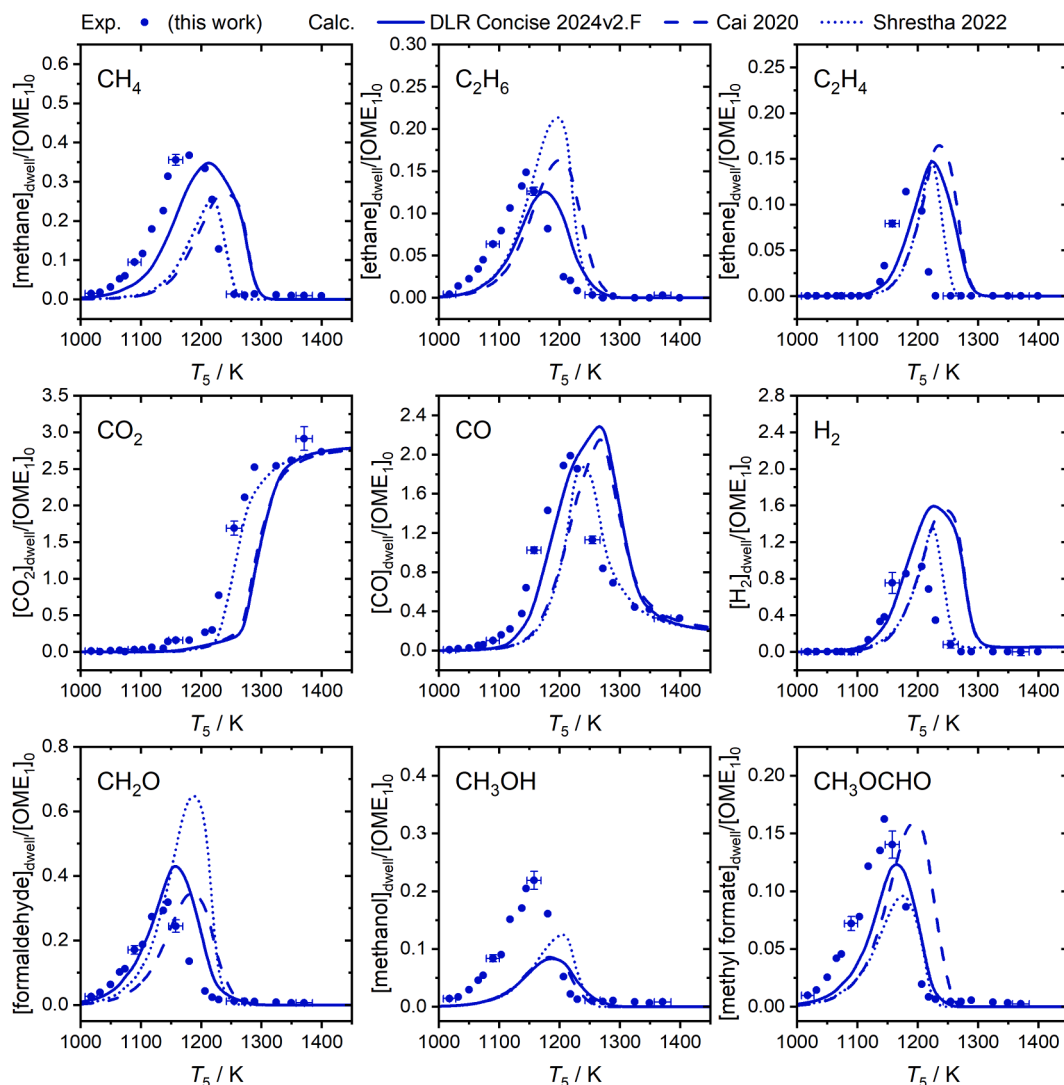

Fig. 12. Normalized species profiles of the decomposition products for the oxidation ($\varphi = 1.0$) of approximately 500 ppm OME_1 diluted in argon with 4950 ppm xenon at pressures around 16 bar. Experiment (this work): Blue circles; calculation: Solid curves (DLRConcise2024v2.F [35]), dashed curves (Cai et al. [47]), and dotted curves (Shrestha et al. [48]).

Regarding the OME$_1$ data measured under oxidative conditions ($\varphi = 1.0$), Fig. 10 shows the mole fraction profiles of OME$_1$ itself, while the corresponding decomposition products are shown in Fig. 12. The temperature shift for OME$_1$ mole fractions between experimental results and model predictions is still observable, since the influence of the additional radicals is low in our experiments due to the high dilution chosen; OME$_1$ is consumed even under oxidative conditions largely via unimolecular decomposition. When comparing the species profiles of OME$_1$ obtained at all three oxidative conditions investigated with those obtained at pyrolytic conditions, a slightly faster decomposition of the fuel is observed as the oxygen content is rising (see Fig. S13 and Fig. S17 for fuel-rich ($\varphi = 2.0$) and fuel-lean ($\varphi = 0.5$) mixtures, respectively). Regarding the methane data, the best match in terms of shape and peak is observed for the prediction of the in-house model DLR Concise [35]; however, Shrestha et al. [48] performs better again as methane starts to be consumed oxidatively. Methane formation is slightly faster for the DLR Concise [35] compared to the other two mechanisms, while the onset in formation of ethane and ethene is being not significantly different in the three model predictions, although they appear slightly slower compared to the experimental data, with some large deviations existing at fuel-rich ($\varphi = 2.0$) conditions.

The CO$_2$, CO, and H$_2$ data are reproduced fairly well, again with some larger deviations at fuel-rich ($\varphi = 2.0$) conditions, especially for CO and H$_2$, and with the predictions of Shrestha et al. [48] performing well once CO and H$_2$ are consumed oxidatively.

Our experimental results for formaldehyde and methyl formate under stoichiometric conditions ($\varphi = 1.0$) are well reproduced by all three reaction mechanisms used, although the mechanism of Shrestha et al. [48] overpredicts the results for formaldehyde. The experimental and modeled results for methyl formate under fuel-lean ($\varphi = 0.5$) conditions are similar to those under stoichiometric conditions ($\varphi = 1.0$), while the results under fuel-rich ($\varphi = 2.0$) conditions appear comparable to those under pyrolytic conditions. Our experimental methanol data do not align with this behavior; instead, the increase in methanol under oxidative conditions is similar to that under pyrolytic conditions, but the decomposition under oxidative conditions starts earlier with increasing oxygen content and is steeper than under pyrolytic conditions.

To discuss the measured and calculated OME$_2$, Fig. 10 shows the mole fractions of OME$_2$ under stoichiometric conditions ($\varphi = 1.0$) while the corresponding decomposition products are given in Fig. 13. The tendency for a slightly faster decomposition with increasing oxygen content already observed for DME and OME$_1$ is also present for OME$_2$. Until complete decomposition of OME$_2$, the temperature difference between the experimental concentration profile at pyrolytic conditions
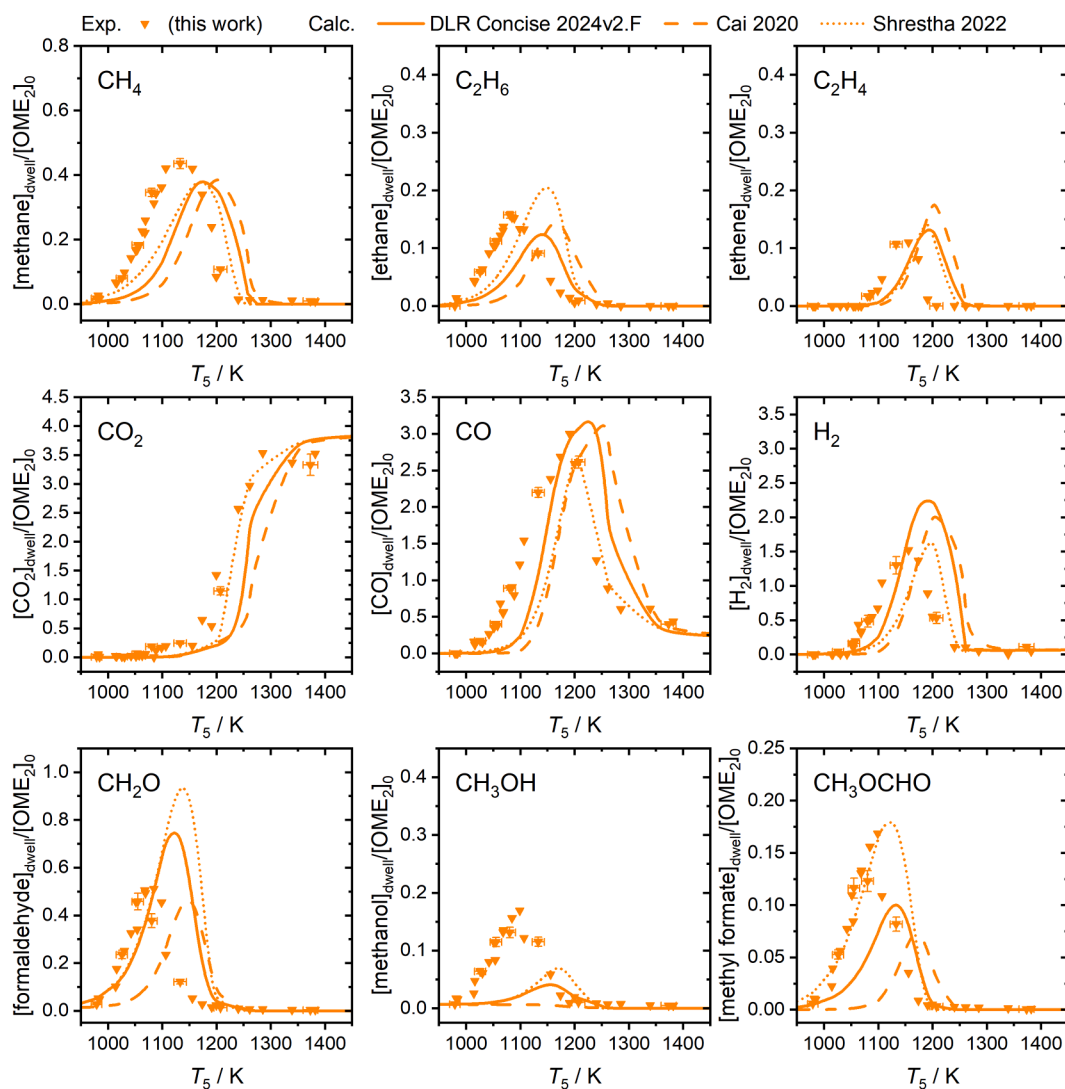

Fig. 13. Normalized species profiles of the decomposition products for the oxidation ($\varphi = 1.0$) of approximately 489 ppm OME$_2$ diluted in argon with 4950 ppm xenon at pressures around 16 bar. Experiment (this work): Orange triangles; calculation: Solid curves (DLRConcise2024v2.F [35]), dashed curves (Cai et al. [47]), and dotted curves (Shrestha et al. [48]).

and those under stoichiometric ($\varphi = 1.0$) and fuel-lean ($\varphi = 0.5$) conditions is approximately 20~K. This observation is also reflected by the reaction mechanisms, albeit to a slightly lesser extent for the model of Shrestha et al. [48].

All three mechanisms perform fairly well considering our methane, ethane and ethene data for all investigated oxidative mixture conditions, but appear also with a slight temperature shift. The same applies to CO_2, CO and H_2, but Shrestha et al. [48] performing best for both CO_2 and CO; however, the predictions of all three mechanisms are slightly over-predicted considering the H_2 data, with Shrestha et al. [48] again being closest to our data.

The behavior of a faster decomposition of methanol with increasing oxygen content already seen within the OME_1 data can also be observed in the OME_2 results. The data for methyl formate is instead comparable for all mixture conditions, while the data for formaldehyde is comparable between fuel-lean ($\varphi = 0.5$) conditions and stoichiometric conditions ($\varphi = 1.0$), as well as between fuel-rich ($\varphi = 2.0$) and pyrolytic conditions.

In conclusion, the temperature difference between the experimental and modeled data of OME_2 compared to those of OME_1 has slightly increased, although the mechanisms generally reproduce the concentration profiles well. Similar to OME_1, the increasing oxygen content has only a minimal influence on the decomposition of OME_2 due to the high dilution but significantly affects the decomposition products. Due to the lack of literature data and the multitude of possible decomposition possibilities, the pathways leading to a decomposition of OME_2 differ markedly between the mechanisms (see ROP Fig. S12). Similar to OME_1, insufficient methanol production by the mechanisms is also observed for the decomposition of OME_2.

6. Summary and conclusions

In this study, we present and provide quantitative data on the speciation of thirteen stable compounds. These were obtained from high pressure single-pulse shock tube experiments involving DME, OME_1, and OME_2. This data is valuable for validating and developing chemical-kinetic reaction mechanisms of these new fuels. The experiments were conducted at pressures of approximately 16 bar and temperatures ranging from 975 K to 1400 K. To the best of our knowledge, no speciation data is yet available for OME_1 and OME_2 in this pressure range. The measurements were carried out behind reflected shock waves for the pyrolysis as well as the oxidation at three different fuel-equivalence ratios $\varphi = 0.5$ (fuel-lean), 1.0 (stoichiometric), and 2.0 (fuel-rich). In addition, to presenting speciation data of DME, OME_1, and OME_2, a customized experimental setup for a single-pulse shock tube has been used. The classical single-pulse mode involving a dump tank was not employed. Instead, post-shock gas samples were collected using a fast-acting solenoid valve that was mounted inside the end flange of the driven section of the shock tube. The temperature behind the reflected shock wave was validated using a chemical thermometry method that measured the thermal decomposition of 1,1,1-trifluoroethane and nitrous oxide, which were then compared with model predictions obtained from literature.

The experimental data of DME, OME_1, and OME_2 have been compared to numerical data calculated by an updated version of the in-house reaction model DLR Concise [35] and by the chemical-kinetic reaction mechanisms by Cai et al. [47] and Shrestha et al. [48], respectively. For DME and OME_1, all three reaction models provide satisfactory and comparable predictions for all the measured species profiles. However, for OME_1, model deviations regarding methanol formation were revealed, that could be worked on in the future. For the OME_2 decomposition, we observed a higher reactivity in the experimental profiles, which we attributed to a slight temperature shift between the experimental and predicted data. This difference was slightly higher in oxidation compared to pyrolysis and could be considered in future model development.

In summary, the presented results offer a collection of high-pressure validation data. This data can enhance the ongoing improvement of chemical-kinetic reaction models for new oxygenated fuels produced from renewable resources. This promotes progress in combustor and engine development for clean combustion by using CFD codes that employ these reaction mechanisms.

CRediT authorship contribution statement

Fabian Lindner: Writing – original draft, Visualization, Validation, Software, Methodology, Investigation, Formal analysis, Data curation, Conceptualization. **Marina Braun-Unkhoff:** Writing – original draft, Supervision, Project administration, Funding acquisition, Formal analysis. **Clemens Naumann:** Writing – review & editing, Supervision, Software, Resources, Project administration, Methodology, Funding acquisition, Formal analysis, Conceptualization. **Torsten Methling:** Writing – review & editing, Software, Formal analysis. **Markus Köhler:** Writing – review & editing, Supervision, Project administration, Funding acquisition. **Uwe Riedel:** Writing – review & editing, Supervision, Project administration, Funding acquisition.

Declaration of competing interest

The authors declare that they have no known competing financial interests or personal relationships that could have appeared to influence the work reported in this paper.

Acknowledgements

Supplementary material

The Supplementary Material (SM) contains pressure profiles that illustrate the post-shock compression pressure rise resulting from gas dynamic effects, along with a figure displaying the time-dependent concentration profile derived from a simulation. ROP analysis for every fuel for pyrolytic and oxidative ($\varphi = 1.0$) conditions is included, as well as the measured species data for the pyrolysis and oxidation at three different fuel-equivalence ratios $\varphi = 0.5$ (fuel-lean), 1.0 (stoichiometric), and 2.0 (fuel-rich) for DME, OME_1, and OME_2. The pressure profiles $p(t)/p_5$ are related to the corresponding species data via the shot number. Species profiles of fuel-lean ($\varphi = 0.5$) and fuel-rich ($\varphi = 2.0$) mixtures of DME, OME_1, and OME_2 are given as figures since they were not shown in the discussion. Furthermore, calculations related to the C/H/O balance for DME, OME_1, and OME_2 are also provided. Species data of 1,1,1-trifluoroethane, 1,1-difluoroethene, and nitrous oxide – as part of our chemical thermometry study – are included and extended via a chi-squared distribution (χ^2) calculation in the form of a table found in an excel spreadsheet, and the corresponding curves as figures.

Supplementary Material associated with this article can be found, in the online version, at doi:10.1016/j.combustflame.2024.113883.

References

[1] United Nations, The Paris Agreement. UN Climate Change Conference (COP21). https://unfccc.int/sites/default/files/english_paris_agreement.pdf (accessed 2023/06/15).

[2] W.F. Lamb, T. Wiedmann, J. Pongratz, R. Andrew, M. Crippa, J.G.J. Olivier, D. Wiedenhofer, G. Mattioli, A.A. Khourdajie, J. House, S. Pachauri, M. Figueroa, Y. Saheb, R. Slade, K. Hubacek, L. Sun, S.K. Ribeiro, S. Khennas, S. de la Rue du Can, L. Chapungu, S.J. Davis, I. Bashmakov, H. Dai, S. Dhakal, X. Tan, Y. Geng, B. Gu, J. Minx, A review of trends and drivers of greenhouse gas emissions by sector from 1990 to 2018, Environ. Res. Lett. 16 (2021) 073005.

[3] P.R. Shukla, J. Skea, A. Reisinger, R. Slade, A. Al Khourdajie, A. Hasija, J. Malley, R. Fradera, M. Belkacemi, G. Lisboa, D. McCollum, M. Pathak, R. van Diemen,

S. Luz, S. Some, P. Vyas, Climate change 2022: mitigation of climate change, in: Working Group III Contribution to the IPCC's Sixth Assessment Report 10, 2022.

[4] R. Prasad, V.R. Bella, A review on diesel soot emission, its effect and control, Bull. Chem. React. Eng. Catal. 5 (2010) 69–86.

[5] D.E. Schraufnagel, The health effects of ultrafine particles, Exp. Mol. Med. 52 (2020) 311–317.

[6] M. Kraft, T. Eikmann, A. Kappos, N. Künzli, R. Rapp, K. Schneider, H. Seitz, J.-U. Voss, H.E. Wichmann, The German view: effects of nitrogen dioxide on human health – derivation of health-related short-term and long-term values, Int. J. Hyg. Environ. Health 208 (2005) 305–318.

[7] K. Kohse-Höinghaus, Combustion in the future: the importance of chemistry, Proc. Combust. Inst. 38 (2021) 1–56.

[8] K. Kohse-Höinghaus, Combustion, chemistry, and carbon neutrality, Chem. Rev. 123 (2023) 5139–5219.

[9] S. Schemme, J.L. Breuer, M. Köller, S. Meschede, F. Walman, R.C. Samsun, R. Peters, D. Stolten, H_2-based synthetic fuels: a techno-economic comparison of alcohol, ether and hydrocarbon production, Int. J. Hydrog. Energy 45 (2020) 5395–5414.

[10] M. Härtl, P. Seidenspinner, E. Jacob, G. Wachtmeister, Oxygenate screening on a heavy-duty diesel engine and emission characteristics of highly oxygenated oxymethylene ether fuel OME_1, Fuel 153 (2015) 328–335.

[11] A. Omari, B. Heuser, S. Pischinger, Potential of oxymethylenether-diesel blends for ultra-low emission engines, Fuel 209 (2017) 232–237.

[12] A. Omari, B. Heuser, S. Pischinger, C. Rüdinger, Potential of long-chain oxymethylene ether and oxymethylene ether-diesel blends for ultra-low emission engines, Appl. Energy 239 (2019) 1242–1249.

[13] S.E. Iannuzzi, C. Barro, K. Boulouchos, J. Burger, Combustion behavior and soot formation/oxidation of oxygenated fuels in a cylindrical constant volume chamber, Fuel 167 (2016) 49–59.

[14] S.L. Fischer, F.L. Dryer, H.J. Curran, The reaction kinetics of dimethyl ether. I: high-temperature pyrolysis and oxidation in flow reactors, Int. J. Chem. Kinet. 32 (2000) 713–740.

[15] H.J. Curran, S.L. Fischer, F.L. Dryer, The reaction kinetics of dimethyl ether. II: low-temperature oxidation in flow reactors, Int. J. Chem. Kinet. 32 (2000) 741–759.

[16] F. Herrmann, P. Oßwald, K. Kohse-Höinghaus, Mass spectrometric investigation of the low-temperature dimethyl ether oxidation in an atmospheric pressure laminar flow reactor, Proc. Combust. Inst. 34 (2013) 771–778.

[17] J.C. Prince, F.A. Williams, A short reaction mechanism for the combustion of dimethyl-ether, Combust. Flame 162 (2015) 3589–3595.

[18] P. Dagaut, C. Daly, J.M. Simmie, M. Cathonnet, The oxidation and ignition of dimethylether from low to high temperature (500–1600 K): experiments and kinetic modeling, Symp. (Int.) Combust. 27 (1998) 361–369.

[19] H. Hashemi, J.M. Christensen, P. Glarborg, High-pressure pyrolysis and oxidation of DME and DME/CH_4, Combust. Flame 205 (2019) 80–92.

[20] A. Stagni, S. Schmitt, M. Pelucchi, A. Frassoldati, K. Kohse-Höinghaus, T. Faravelli, Dimethyl ether oxidation analyzed in a given flow reactor: experimental and modeling uncertainties, Combust. Flame 240 (2022) 111998.

[21] C. Yan, H. Zhao, Z. Wang, G. Song, Y. Lin, C.R. Mulvihill, A.W. Jasper, S. J. Klippenstein, Y. Ju, Low-and intermediate-temperature oxidation of dimethyl ether up to 100 atm in a supercritical pressure jet-stirred reactor, Combust. Flame 243 (2022) 112059.

[22] N. Gaiser, T. Bierkandt, P. Oßwald, J. Zinsmeister, T. Kathrotia, S. Shaqiri, P. Hemberger, T. Kasper, M. Aigner, M. Köhler, Oxidation of oxymethylene ether (OME_{0-5}): an experimental systematic study by mass spectrometry and photoelectron photoion coincidence spectroscopy, Fuel 313 (2022) 122650.

[23] N. Gaiser, H. Zhang, T. Bierkandt, S. Schmitt, J. Zinsmeister, T. Kathrotia, P. Hemberger, S. Shaqiri, T. Kasper, M. Aigner, P. Oßwald, M. Köhler, Investigation of the combustion chemistry in laminar, low-pressure oxymethylene ether flames (OME_{0-4}), Combust. Flame 243 (2022) 112060.

[24] J.M. Ngugi, S. Richter, M. Braun-Unkhoff, C. Naumann, U. Riedel, An investigation of fundamental combustion properties of the oxygenated fuels DME and OME_1, in: ASME Turbo Expo, 2020. GT2020-14702.

[25] J.M. Ngugi, S. Richter, M. Braun-Unkhoff, C. Naumann, M. Köhler, U. Riedel, A study on fundamental combustion properties of oxymethylene ether-2, J. Eng. Gas Turbines Power 144 (2022) 011014.

[26] J.M. Ngugi, S. Richter, M. Braun-Unkhoff, C. Naumann, U. Riedel, A study on fundamental combustion properties of oxymethylene ether-1, the primary reference fuel 90, and their blend: experiments and modeling, Combust. Flame 243 (2022) 111996.

[27] N. Gaiser, T. Bierkandt, P. Oßwald, J. Zinsmeister, P. Hemberger, S. Shaqiri, M. Aigner, T. Kasper, M. Köhler, Oxidation of linear and branched ethers: a comparative flow reactor study of OME_2 and trimethoxymethane, Proc. Combust. Inst. 39 (2023) 685–693.

[28] M. Döntgen, M.E. Fuller, S. Peukert, D. Nativel, C. Schulz, K.A. Heufer, C. F. Goldsmith, Shock tube study of the pyrolysis kinetics of Di- and trimethoxy methane, Combust. Flame 242 (2022) 112186.

[29] L. Marrodán, E. Royo, Á. Millera, R. Bilbao, M.U. Alzueta, High pressure oxidation of dimethoxymethane, Energy Fuels 29 (2015) 3507–3517.

[30] S. Richter, T. Kathrotia, M. Braun-Unkhoff, C. Naumann, M. Köhler, Influence of oxymethylene ethers (OME_n) in mixtures with a diesel surrogate, Energies 14 (2021) 7848.

[31] H. Wang, Z. Yao, X. Zhong, Q. Zuo, Z. Zheng, Y. Chen, M. Yao, Experimental and kinetic modeling studies on low-temperature oxidation of Polyoxymethylene

[32] R. Schmitz, C. Russo, F. Ferraro, B. Apicella, M. Hasse, M. Sirignano, Effect of oxymethylene ether-2-3-4 (OME_{2-4}) on soot particle formation and chemical features, Fuel 324 (2022) 124617.

[33] D.F. Schuler, C. Naumann, M. Braun-Unkhoff, U. Riedel, F. Zabel, A single pulse shock tube study on the pyrolysis of 2,5-dimethylfuran, Z. Phys. Chem. 229 (2015) 529–548.

[34] A. Lifshitz, S.H. Bauer, E.L. Resler Jr., Studies with a single-pulse shock tube. I. The Cis—Trans isomerization of butene-2, J. Chem. Phys. 38 (1963) 2056–2063.

[35] T. Kathrotia, T. Bierkandt, N. Gaiser, S. Richter, F. Lindner, S. Jacobs, C. Naumann, T. Methling, P. Oßwald, M. Köhler, Combustion kinetics of alternative fuels, Part-IV: extending reaction mechanism "DLR Concise" to include oxygenates for transportation fuels, Combust. Flame 271 (2025) 113841.

[36] G. Ben-Dor, O. Igra, T. Elperin, Handbook of Shock Waves, Three Volume Set, Academic Press, 2001.

[37] C.T. Bowman, R.K. Hanson, Shock tube measurements of rate coefficients of elementary gas reactions, J. Phys. Chem. 83 (1979) 757–763.

[38] E.C. Voldner, O. Trass, Evaluation of thermal boundary layer interaction in shock tube sampling for kinetic studies, J. Chem. Phys. 73 (1980) 1601–1611.

[39] A. Lifshitz, A. Bar-Nun, P.C.T. de Boer, E.L. Resler Jr., Boundary layer effects on chemical kinetics studies in a shock tube, J. Chem. Phys. 53 (1970) 3050–3055.

[40] A.M. Ferris, J.W. Streicher, A.J. Susa, D.F. Davidson, R.K. Hanson, A comparative laser absorption and gas chromatography study of low-temperature n-heptane oxidation intermediates, Proc. Combust. Inst. 37 (2019) 249–257.

[41] X. Han, J.M. Mehta, K. Brezinsky, Temperature approximations in chemical kinetics studies using single pulse shock tubes, Combust. Flame 209 (2019) 1–12.

[42] Y. Hidaka, T. Nakamura, A. Miyauchi, T. Shiraishi, H. Kawano, Thermal decomposition of propyne and allene in shock waves, Int. J. Chem. Kinet. 21 (1989) 643–666.

[43] W. Tsang, A. Lifshitz, Shock tube techniques in chemical kinetics, Annu. Rev. Phys. Chem. 41 (1990) 559–599.

[44] A.E. Lutz, R.J. Kee, J.A. Miller, SENKIN: A Fortran Program for Predicting Homogeneous Gas Phase Chemical Kinetics With Sensitivity Analysis, Sandia National Laboratories, CA (USA), 1988.

[45] T. Kathrotia, P. Oßwald, C. Naumann, S. Richter, M. Köhler, Combustion kinetics of alternative jet fuels, Part-II: Reaction model for fuel surrogate, Fuel 302 (2021) 120736.

[46] P. Glarborg, J.A. Miller, B. Ruscic, S.J. Klippenstein, Modeling nitrogen chemistry in combustion, Prog. Energy Combust. Sci. 67 (2018) 31–68.

[47] L. Cai, S. Jacobs, R. Langer, F. vom Lehn, K.A. Heufer, H. Pitsch, Auto-ignition of oxymethylene ethers (OMEn, n = 2–4) as promising synthetic e-fuels from renewable electricity: shock tube experiments and automatic mechanism generation, Fuel 264 (2020) 116711.

[48] K.P. Shrestha, S. Eckart, S. Drost, C. Fritsche, R. Schießl, L. Seidel, U. Maas, H. Krause, F. Mauss, A comprehensive kinetic modeling of oxymethylene ethers (OMEn, n=1–3) oxidation - laminar flame speed and ignition delay time measurements, Combust. Flame 246 (2022) 112426.

[49] W. Tsang, Comparative rate single pulse shock tube in the thermal stability of polyatomic molecules, in: A. Lifshitz (Ed.), Shock Tubes in Chemistry, Marcel Dekker, New York, 1981, p. 59.

[50] A. Lifshitz, The single pulse shock tube: its Odyssey in chemical kinetics, in: Z. Jiang (Ed.), Shock Waves, Springer, Berlin, Heidelberg, 2005, pp. 57–64.

[51] P.T. Lynch, G. Wang, Chemical thermometry in miniature HRRST using 1,1,1-trifluoroethane dissociation, Proc. Combust. Inst. 36 (2017) 307–314.

[52] P. Sela, B. Shu, M. Aghsaee, J. Herzler, O. Welz, M. Fikri, C. Schulz, A single-pulse shock tube coupled with high-repetition-rate time-of-flight mass spectrometry and gas chromatography for high-temperature gas-phase kinetics studies, Rev. Sci. Instrum. 87 (2016) 105103.

[53] R.S. Tranter, R. Sivaramakrishnan, N. Srinivasan, K. Brezinsky, Calibration of reaction temperatures in a very high pressure shock tube using chemical thermometers, Int. J. Chem. Kinet. 33 (2001) 722–731.

[54] B. Sirjean, R. Fournet, P.-A. Glaude, F. Battin-Leclerc, W. Wang, M. A. Oehlschlaeger, Shock tube and chemical kinetic modeling study of the oxidation of 2,5-dimethylfuran, J. Phys. Chem. A 117 (2013) 1371–1392.

[55] J.M. Mehta, K. Brezinsky, Experimental speciation study of natural gas oxidation using a single pulse shock tube, Int. J. Chem. Kinet. 53 (2021) 845–867.

[56] W. Tang, K. Brezinsky, Chemical kinetic simulations behind reflected shock waves, Int. J. Chem. Kinet. 38 (2006) 75–97.

[57] A. Fridlyand, P.T. Lynch, R.S. Tranter, K. Brezinsky, Single pulse shock tube study of allyl radical recombination, J. Phys. Chem. A 117 (2013) 4762–4776.

[58] A. Lifshitz, C. Tamburu, R. Shashua, Thermal decomposition of 2,5-dimethyl-furan. Experimental results and computer modeling, J. Phys. Chem. A 102 (1998) 10655–10670.

[59] A. Lifshitz, C. Tamburu, F. Dubnikova, Reactions of 1-naphthyl radicals with acetylene. Single-Pulse shock tube experiments and quantum chemical calculations. Differences and similarities in the reaction with ethylene, J. Phys. Chem. A 113 (2009) 10446–10451.

[60] D.L. Baulch, C.T. Bowman, C.J. Cobos, R.A. Cox, T. Just, J.A. Kerr, M.J. Pilling, D. Stocker, J. Troe, W. Tsang, R.W. Walker, J. Warnatz, Evaluated kinetic data for combustion modeling: supplement II, J. Phys. Chem. Ref. Data 34 (2005) 757–1397.

[61] J.E. Johnsson, P. Glarborg, K. Dam-Johansen, Thermal dissociation of nitrous oxide at medium temperatures, Symp. (Int.) Combust. 24 (1992) 917–923.

[62] A.A. Konnov, An exploratory modelling study of chemiluminescence in ammonia-fuelled flames. Part 2, Combust. Flame 253 (2023) 112789.

[63] W. Tsang, A. Lifshitz, Kinetic stability of 1,1,1-trifluoroethane, Int. J. Chem. Kinet. 30 (1998) 621–628.

[64] J.H. Kiefer, C. Katopodis, S. Santhanam, N.K. Srinivasan, R.S. Tranter, A shock-tube, laser-schlieren study of the dissociation of 1,1,1-trifluoroethane: an intrinsic non-RRKM process, J. Phys. Chem. A 108 (2004) 2443–2450.

[65] B.R. Giri, R.S. Tranter, Dissociation of 1,1,1-trifluoroethane behind reflected shock waves: shock tube/time-of-flight mass spectrometry experiments, J. Phys. Chem. A 111 (2007) 1585–1592.

[66] K. Takahashi, A. Harada, S. Horigome, R. Cho, T. Inomata, Thermal decompositons of 1,1,1-trifluoroethane and pentafluoroethane in a turbulent flow reactor, Combust. Sci. Technol. 179 (2007) 1417–1432.

[67] A. Matsugi, K. Yasunaga, H. Shiina, Thermal decomposition of 1,1,1-trifluoro-ethane revisited, J. Phys. Chem. A 118 (2014) 11688–11695.

[68] A. Matsugi, Dissociation of 1,1,1-trifluoroethane is an intrinsic RRKM process: classical trajectories and successful master equation modeling, J. Phys. Chem. A 119 (2015) 1846–1858.

[69] E. Tschuikow-Roux, W.J. Quiring, Kinetics of the thermally induced dehydrofluorination of 1, 1, 1-trifluoroethane in shock waves, J. Phys. Chem. 75 (1971) 295–300.

[70] X. Han, A Shock Tube Study of the Pyrolysis of Real Jet Fuels Jet A and JP10, University of Illinois at Chicago, USA, 2018.

[71] D.F. Schuler, Validierung von Reaktionsmechanismen für biogene Kraftstoffkomponenten, University of Stuttgart, Germany, 2016.

[72] J.M. Simmie, E. Tschuikow-Roux, Kinetics of the Shock-initiated decomposition of 1,1-difluoroethylene, J. Phys. Chem. 74 (1970) 4075–4079.

[73] P.R. Bevington, D.K. Robinson, Data Reduction and Error Analysis for the Physical Sciences, McGraw-Hill, 2003.

[74] E. Goos, A. Burcat, B. Ruscic, Extended third millenium ideal gas thermochemical database with updates from active thermochemical tables. http://burcat.tech nion.ac.il/dir; (accessed 2023/02/27). mirrored at http://garfield.chem.elte.hu /Burcat/burcat.html (accessed 2023/02/27).

[75] C.D. Johnson, D. Britton, Shock waves in chemical kinetics: the use of reflected shock waves, J. Chem. Phys. 38 (1963) 1455–1462.

[76] W. Sun, G. Wang, S. Li, R. Zhang, B. Yang, J. Yang, Y. Li, C.K. Westbrook, C. K. Law, Speciation and the laminar burning velocities of poly(oxymethylene) dimethyl ether 3 (POMDME$_3$) flames: an experimental and modeling study, Proc. Combust. Inst. 36 (2017) 1269–1278.

[77] A. Rodriguez, O. Frottier, O. Herbinet, R. Fournet, R. Bounaceur, C. Fittschen, F. Battin-Leclerc, Experimental and modeling investigation of the low-temperature oxidation of dimethyl ether, J. Phys. Chem. A 119 (2015) 7905–7923.

[78] L. Golka, D. Gratzfeld, I. Weber, M. Olzmann, Temperature-and pressure-dependent kinetics of the competing C–O bond fission reactions of dimethoxymethane, Phys. Chem. Chem. Phys. 22 (2020) 5523–5530.

[79] R. Sivaramakrishnan, J.V. Michael, A.F. Wagner, R. Dawes, A.W. Jasper, L. B. Harding, Y. Georgievskii, S.J. Klippenstein, Roaming radicals in the thermal decomposition of dimethyl ether: experiment and theory, Combust. Flame 158 (2011) 618–632.

[80] U. Burke, K.P. Somers, P. O'Toole, C.M. Zinner, N. Marquet, G. Bourque, E. L. Petersen, W.K. Metcalfe, Z. Serinyel, H.J. Curran, An ignition delay and kinetic modeling study of methane, dimethyl ether, and their mixtures at high pressures, Combust. Flame 162 (2015) 315–330.

[81] B. Wang, H. Hou, L.M. Yoder, J.T. Muckerman, C. Fockenberg, Experimental and theoretical investigations on the methyl–methyl recombination reaction, J. Phys. Chem. A 107 (2003) 11414–11426.

[82] M.A. Oehlschlaeger, D.F. Davidson, R.K. Hanson, High-temperature ethane and propane decomposition, Proc. Combust. Inst. 30 (2005) 1119–1127.

[83] M.P. Burke, F.L. Dryer, Y. Ju, Assessment of kinetic modeling for lean H$_2$/CH$_4$/O$_2$/diluent flames at high pressures, Proc. Combust. Inst. 33 (2011) 905–912.

[84] G. Blanquart, P. Pepiot-Desjardins, H. Pitsch, Chemical mechanism for high temperature combustion of engine relevant fuels with emphasis on soot precursors, Combust. Flame 156 (2009) 588–607.

[85] K.P. Shrestha, L. Seidel, T. Zeuch, F. Mauss, Detailed kinetic mechanism for the oxidation of ammonia including the formation and reduction of nitrogen oxides, Energy Fuels 32 (2018) 10202–10217.

[86] K.P. Shrestha, L. Seidel, T. Zeuch, F. Mauss, Kinetic modeling of NO$_x$ formation and consumption during methanol and ethanol oxidation, Combust. Sci. Technol. 191 (2019) 1627–1659.

[87] G. Friedrichs, D.F. Davidson, R.K. Hanson, Validation of a thermal decomposition mechanism of formaldehyde by detection of CH$_2$O and HCO behind shock waves, Int. J. Chem. Kinet. 36 (2004) 157–169.

[88] E.A. Irdam, J.H. Kiefer, L.B. Harding, A.F. Wagner, The formaldehyde decomposition chain mechanism, Int. J. Chem. Kinet. 25 (1993) 285–303.

[89] T.M. Pazdera, J. Wenz, M. Olzmann, The unimolecular decomposition of dimethoxymethane: channel switching as a function of temperature and pressure, Faraday Discuss. 238 (2022) 665–681.

[90] T. He, Z. Wang, X. You, H. Liu, Y. Wang, X. Li, X. He, A chemical kinetic mechanism for the low-and intermediate-temperature combustion of Polyoxymethylene Dimethyl Ether 3 (PODE$_3$), Fuel 212 (2018) 223–235.

[91] K. De Ras, M. Kusenberg, G. Vanhove, Y. Fenard, A. Eschenbacher, R.J. Varghese, J. Aerssens, R. Van de Vijver, L.-S. Tran, J.W. Thybaut, K.M. Van Geem, A detailed experimental and kinetic modeling study on pyrolysis and oxidation of oxymethylene ether-2 (OME-2), Combust. Flame 238 (2022) 111914.

[92] L. Golka, Kinetische Untersuchungen zur Pyrolyse oxygenierter Kohlenwasserstoffe: Stoßwellenexperimente und Kinetische Modellierungen, Karlsruhe Institute of Technology (KIT), Germany, 2019.

[93] S. Jacobs, M. Döntgen, A.B.S. Alquaity, W.A. Kopp, L.C. Kröger, U. Burke, H. Pitsch, K. Leonhard, H.J. Curran, K.A. Heufer, Detailed kinetic modeling of dimethoxymethane. Part II: experimental and theoretical study of the kinetics and reaction mechanism, Combust. Flame 205 (2019) 522–533.

[94] K.P. Shrestha, S. Eckart, A.M. Elbaz, B.R. Giri, C. Fritsche, L. Seidel, W.L. Roberts, H. Krause, F. Mauss, A comprehensive kinetic model for dimethyl ether and dimethoxymethane oxidation and NO$_x$ interaction utilizing experimental laminar flame speed measurements at elevated pressure and temperature, Combust. Flame 218 (2020) 57–74.

[95] F.H. Vermeire, H.-H. Carstensen, O. Herbinet, F. Battin-Leclerc, G.B. Marin, K. M. Van Geem, Experimental and modeling study of the pyrolysis and combustion of dimethoxymethane, Combust. Flame 190 (2018) 270–283.

[96] W. Sun, T. Tao, M. Lailliau, N. Hansen, B. Yang, P. Dagaut, Exploration of the oxidation chemistry of dimethoxymethane: Jet-stirred reactor experiments and kinetic modeling, Combust. Flame 193 (2018) 491–501.

[97] S. Peukert, P. Sela, D. Nativel, J. Herzler, M. Fikri, C. Schulz, Direct measurement of high-temperature rate constants of the thermal decomposition of dimethoxymethane, a shock tube and modeling study, J. Phys. Chem. A 122 (2018) 7559–7571.

[98] K. De Ras, M. Kusenberg, J.W. Thybaut, K.M. Van Geem, Unraveling the carbene chemistry of oxymethylene ethers: Experimental investigation and kinetic modeling of the high-temperature pyrolysis of OME-2, Proc. Combust. Inst. 39 (2023) 125–133.

[99] C. Zhang, J. He, Y. Li, X. Li, P. Li, Ignition delay times and chemical kinetics of diethoxymethane/O$_2$/Ar mixtures, Fuel 154 (2015) 346–351.

[100] K. Yasunaga, F. Gillespie, J.M. Simmie, H.J. Curran, Y. Kuraguchi, H. Hoshikawa, M. Yamane, Y. Hidaka, A multiple shock tube and chemical kinetic modeling study of diethyl ether pyrolysis and oxidation, J. Phys. Chem. A 114 (2010) 9098–9109.

[101] M.P. Burke, M. Chaos, Y. Ju, F.L. Dryer, S.J. Klippenstein, Comprehensive H$_2$/O$_2$ kinetic model for high-pressure combustion, Int. J. Chem. Kinet. 44 (2012) 444–474.

[102] Z. Hong, D.F. Davidson, K.-Y. Lam, R.K. Hanson, A shock tube study of the rate constants of HO$_2$ and CH$_3$ reactions, Combust. Flame 159 (2012) 3007–3013.